Draft version December 14, 2016
Preprint typeset using LaTeX style emulateapj v. 5/2/11

arXiv:1612.04020v1 [astro-ph.GA] 13 Dec 2016

CONSTRAINING THE STELLAR POPULATIONS AND STAR FORMATION HISTORIES OF BLUE COMPACT DWARF GALAXIES WITH SED FITS

Steven Janowiecki[1,2], John J. Salzer[2], Liese van Zee[2], Jessica L. Rosenberg[3], Evan Skillman[4]

(Received 15 Sep 2016; Accepted 12 Dec 2016)
Draft version December 14, 2016

ABSTRACT

We discuss and test possible evolutionary connections between Blue Compact Dwarf galaxies (BCDs) and other types of dwarf galaxies. BCDs provide ideal laboratories to study intense star formation episodes in low mass dwarf galaxies, and have sometimes been considered a short-lived evolutionary stage between types of dwarf galaxies. To test these connections, we consider a sample of BCDs as well as a comparison sample of nearby galaxies from the Local Volume Legacy (LVL) survey for context. We fit the multi-wavelength spectral energy distributions (SED, far-ultra-violet to far-infrared) of each galaxy with a grid of theoretical models to determine their stellar masses and star formation properties. We compare our results for BCDs with the LVL galaxies to put BCDs in the context of normal galaxy evolution. The SED fits demonstrate that the star formation events currently underway in BCDs are at the extreme of the continuum of normal dwarf galaxies, both in terms of the relative mass involved and in the relative increase over previous star formation rates. Today's BCDs are distinctive objects in a state of extreme star formation which is rapidly transforming them. This study also suggests ways to identify former BCDs whose star formation episodes have since faded.

1. INTRODUCTION

The formation and evolutionary pathways of dwarf galaxies are still not well-understood, despite the fact that they are fairly simple systems and are the most abundant type of galaxy in the universe. Many studies have focused on the idea that dwarf galaxy evolution is driven by interactions and mergers, through ram pressure stripping, tidal disruption, or other external transformations. Today, there are many well-established mechanisms to evolve dwarf galaxies in high density group and cluster environments. It has been more difficult to study the ongoing secular dwarf galaxy evolution in isolated environments where mergers and interactions have a smaller impact. In this regime, star formation is the most transformative process a dwarf galaxy can undergo.

The best places to study the transformative effects of star formation are in the dwarf galaxies with the highest star formation rates (SFRs): the Blue Compact Dwarf galaxies (BCDs). Dwarf galaxies are often broadly categorized as either dwarf irregulars (dIs) which lack a regular morphology, possess substantial gas reservoirs, and are often forming stars, or as dwarf spheroidals (dSphs, or dwarf ellipticals, dEs), which have regular isophotes, are gas-poor, and are not forming stars. BCDs are classified in a variety of ways, but are observationally remarkable for their strong emission lines and star formation (Sargent & Searle 1970; Searle & Sargent 1972; Izotov & Thuan 2004), their underlying old stellar population (Loose & Thuan 1986; Aloisi et al. 2007), their exceptionally low gas-phase metallicity (Terlevich et al. 1991; Izotov et al. 1994; Izotov & Thuan 1999; Hunter & Hoffman 1999), and their compact underlying stellar and HI distributions (Papaderos et al. 1996; van Zee et al. 1998; Janowiecki & Salzer 2014; Lelli et al. 2014). Some groups have hypothesized that a compact mass distribution is the most distinctive characteristic of a BCD (van Zee et al. 1998; Lelli et al. 2014; McQuinn et al. 2015c).

Recently, many groups have used observations to study the evolutionary connections between BCDs and other dwarf galaxies. Detailed studies of individual extreme objects (e.g., Guseva et al. 2001; Ashley et al. 2014) and systematic surveys of many objects (e.g., Noeske et al. 2007) have both suggested that BCDs are members of a rapidly evolving class of galaxies, and play an important role in dwarf galaxy evolution. Deep surface photometry studies (Noeske et al. 2003, 2005) in addition to spectroscopic observations (Papaderos et al. 2008) have highlighted the possible connections between BCDs and dwarf irregulars in terms of their structural parameters and chemical evolution. Other observations suggest that the unusually low metallicity of BCDs is more likely maintained by outflows of enriched winds (Carigi et al. 1995; Mac Low & Ferrara 1999; McQuinn et al. 2015b) rather than pristine gas infall (Matteucci & Chiosi 1983). There have also been efforts to find galaxies which may have experienced a BCD-like star formation event at some point in their history, or to predict the future evolutionary state of today's BCDs (Sánchez Almeida et al. 2008, 2009; Amorín et al. 2012; Lelli et al. 2012; Koleva et al. 2013; Meyer et al. 2014).

One of the big questions about BCDs is the reason for their intense star formation, and whether they have been triggered in some way. There are well-studied examples where mergers or interactions between dIs have externally triggered intense star formation (e.g.,

steven.janowiecki@uwa.edu.au
[1] International Center for Radio Astronomy Research, M468, The University of Western Australia, 35 Stirling Highway, Crawley, Western Australia, 6009, Australia
[2] Department of Astronomy, Indiana University, 727 East Third Street, Bloomington, IN 47405, USA
[3] Department of Physics and Astronomy, George Mason University, Fairfax, VA 22030, USA
[4] Minnesota Institute for Astrophysics, University of Minnesota, 116 Church Street, SE Minneapolis, MN, 55455 USA

II Zw 40, Sargent & Searle 1970; Baldwin et al. 1982; Terlevich et al. 1991; van Zee et al. 1998; Bordalo et al. 2009). Recently, cosmologically-relevant hydrodynamical simulations are beginning to approach these questions from a theoretical perspective (e.g., Valcke et al. 2008, and references therein). While dwarf-dwarf galaxy mergers become increasingly rare at lower masses (Deason et al. 2014), some groups have had success in producing BCD-like galaxies through these interactions (Bekki 2008). Others have considered the effects of in-spiraling star-forming clumps in dwarf galaxies (Elmegreen et al. 2012), or the interaction between a dwarf galaxy and an infalling cloud of gas (Verbeke et al. 2014), both of which can reproduce some of the observed properties of BCDs. Both the merger and gas infall scenarios frequently result in substantial structural changes to the simulated galaxies, and represent extreme transformations in the life of a dI. However, in this work we focus on the internal secular evolution of isolated BCDs, and avoid discussing mergers and interactions.

Compared with typical dIs, BCDs have been found to be especially compact, in their underlying stellar and HI distributions (Papaderos et al. 1996; van Zee et al. 1998; Janowiecki & Salzer 2014; Lelli et al. 2014). This compactness may be related to their ability to host such intense starbursts. When parametrizing the strength of a star-forming event, the birthrate parameter (b=SFR/$\langle$SFR$\rangle$, see Section 4.2) is often used, which compares the current star formation with the lifetime average. In the local universe, intense star-forming galaxies are rare as only $\sim$1% of star-forming galaxies are considered starbursts with $b \geq 3$ (Bergvall et al. 2015). When combining this rarity with the stochastic nature of star-formation in dwarf galaxies (e.g., Lee et al. 2009; Weisz et al. 2012; Bauer et al. 2013), it would appear that dwarf galaxies can experience increases and decreases in their star formation rate, and only a small fraction are starbursting at any given time. Perhaps the especially-compact BCDs are able to burst more effectively than typical dIs, and so can reach higher SFR during their periods of starburst.

To compare the star formation properties and evolutionary history of BCDs and dIs from the Local Volume Legacy survey (LVL, Dale et al. 2009), we consider the wealth of information contained in their stellar populations. An understanding of these stellar populations can constrain the amount and impact of recent and past star-formation activity. We have obtained multi-wavelength photometry in order to fit the spectral energy distributions (SEDs) for the BCDs and LVL galaxies. SED fitting has recently become a widely-used tool to derive physical properties of galaxies, including their stellar masses and star formation rates (cf., Walcher et al. 2011).

Given that stellar mass is often considered the most fundamental parameter driving a galaxy's evolutionary path (e.g., Tremonti et al. 2004; Kewley & Ellison 2008, and references therein), star forming galaxies are often plotted on a "main sequence", analogously to the main sequence of stellar evolution. This correlation between the stellar masses and SFRs of star-forming galaxies has been observed for massive galaxies in the nearby universe (Brinchmann et al. 2004; Salim et al. 2007) and at higher redshift (Daddi et al. 2007), with a scatter of only $\sim$0.2 dex. The fact that this relationship exists with such low scatter across a wide range of redshifts seems to imply a universal mode of star formation, from which galaxies rarely deviate (Noeske et al. 2007). At smaller masses (below $10^9 M_\odot$) the scatter becomes larger, as episodic bursts of star formation can affect dwarf galaxies more significantly (e.g., Cook et al. 2014b; McQuinn et al. 2010a; Weisz et al. 2011).

Galaxy stellar masses are most commonly determined by converting observed luminosities to masses (e.g., Bell & de Jong 2001; McGaugh & Schombert 2014). Often a color (e.g., B$-$V), is used to determine the mass-to-light ratio, but these estimates become less reliable for galaxies which deviate from mean scaling relations (e.g., if they are currently experiencing a starburst). In order to more uniformly determine stellar masses across our sample of BCDs and LVL galaxies, a full multi-wavelength SED-fit is necessary.

Our SED fits can be also used to make crude estimates of the SFR and star formation histories (SFHs) for BCDs and LVL galaxies, which describe the amount of star formation they experienced throughout their lifetimes. Different observational indicators are sensitive to star formation of different ages, and the SED fits incorporate all of the multi-wavelength information into a single best fitting SFH. While the broadband photometry can never produce as accurate and well-constrained a SFH as resolved stellar photometry (e.g., Tolstoy et al. 2009; McQuinn et al. 2010a, 2015a), it can still be useful in comparing BCDs with typical LVL galaxies. In particular, the stellar masses and SFRs from the SED fits allow us to quantify how extreme the BCDs are compared with typical LVL galaxies, and to constrain the possible evolutionary connections between BCDs and other dwarf galaxies.

This paper is organized as follows. In Section 2, we describe the multi-wavelength photometric observations of the BCDs and comparison samples. In Section 3 we discuss our SED-fitting methods and the consistency checks and verifications of our results. In Section 4 we show the results of our best SED fits. Section 5 contains a discussion of these results and their implications, and we briefly summarize our main findings in Section 6.

2. OBSERVATIONAL DATA

Our primary sample of 18 actively star-forming galaxies is the same as that of Janowiecki & Salzer (2014), and includes a variety of BCDs and related galaxies. Some are canonical BCDs (e.g., I Zw 18), while some have smooth outer isophotes (similar to a dE) with a strong central starburst (e.g., Mk 900). Some have offset starbursts (e.g., Mk 36, Mk 750), dual starburst regions (UM 461, Mk 600), cometary shapes (Mk 5), or large numbers of active star formation sites (e.g., UM 439, UM 462, UM 323). Our sample is faint ($\langle M_B \rangle = -16$ mag), blue ($0 < B-V < 0.5$), metal deficient ($\langle 12+\log(O/H) \rangle \sim 8$), and less than 50 Mpc away (see Table 1 in Janowiecki & Salzer 2014, for more details).

Our BCD sample is not comprehensive, but instead is representative and its members span the range of parameter space that BCDs typically occupy. Samples of BCDs have been defined in various ways, beginning from their identification as extragalactic HII regions (Sargent & Searle 1970), continuing through the definitions of Thuan & Martin (1981) and Gil de Paz et al.

TABLE 1
Photometric observations of the BCD sample

Galaxy	*GALEX*	U	B	V	R	I	Hα	J	H	K_s	Spitzer
UM 323	F/N		SN/W	W	W	SN	SN	SN/W	SN/W	W	
UM 408	F/N		SN/W	W	W	SN	SN	SN/W	SN/W	W	
Mk 600	F/N		SN/W	W	W	SN	SN	SN/W	SN/W	SN/W	I/M
II Zw 40	F/N	SN	SN	SN	SN	SN	SN	SN	SN	SN	I/M
Mk 5	F/N	SN	SN/W	SN	W	SN	SN	SN	SN	SN	I/M
CG 10	F/N		W	W	W			W	W	W	
I Zw 18	F/N	SN	SN	SN	SN		SN	SN	SN	SN	I/M
Was 5	F/N	SN	SN	SN	W		SN	SN	SN	SN	
Mk 36	F/N	SN	SN	SN	W		SN	SN	SN	SN	I/M
UM 439	F/N	SN	SN	SN	W		SN	SN	SN	SN	
Mk 750		SN	SN	SN	W		SN	SN	SN	SN	
UM 461	N	SN	SN	SN	W		SN	SN	SN	SN	I/M
UM 462	F/N	SN	SN	SN	W		SN	SN	SN	SN	I/M
Mk 67	F/N	SN	SN	SN	SN	SN	SN	SN	SN	SN	I
Mk 475	F/N	SN	SN	SN	W		SN	SN	SN	SN	I/M
Mk 900	F/N		SN/W	W	W	SN	SN	SN	SN	SN	I/M
Mk 324	F/N	SN	SN/W	SN	SN/W	SN	SN	SN	SN	SN	
Mk 328	F/N	SN	SN/W	SN	SN/W	SN	SN	SN	SN	SN	

Note. — F/N - FUV and NUV *GALEX* observations; SN - Sudarsky (1995) & Norton (1997); W - WIYN 3.5m observations; I-IRAC, M-MIPS;

(2003). All of these samples commonly include dwarf galaxies which are compact (or merely small) and intensely forming stars. However, conclusions about the evolution of BCDs can depend strongly on sample selection (see also Section 5 of Janowiecki & Salzer 2014). Rather than creating or adopting a definition of BCDs, we instead select a sample of BCDs and BCD-like galaxies to study the extremes of dwarf galaxy evolution.

Toward this end, we include the galaxies in the Local Volume Legacy (LVL) survey as a comparison sample. LVL is a volume-limited survey of 258 galaxies within 11 Mpc, which includes flux observations from the ultraviolet to the far-infrared. The LVL sample is a particularly good comparison sample as its volume limited nature means that a majority of its galaxies have stellar masses below $10^9 M_\odot$, similar to our BCD sample (Dale et al. 2009). In fact, some of the galaxies in the LVL sample are classified as BCDs, as discussed in Section 2.3. In this analysis, we do not consider the environment of LVL galaxies (or BCDs), and treat each galaxy individually; further work is needed to explore the effects of the environment on star formation processes in dwarf galaxies.

2.1. *Photometric observations of the BCD sample*

The multi-wavelength photometric observations of our BCD sample come from many sources. Table 1 shows a complete summary of the photometry for each object, and Table 2 contains all of the observed fluxes of our BCD sample. We also use gas-phase abundances from spectroscopic observations of the BCDs from sources in the literature (Zhao et al. 2010; Brinchmann et al. 2008; Izotov et al. 2007). These abundances allow us to consider the chemical evolution of the BCDs and put them in context of galaxy scaling relations.

In the UV, we use far-ultraviolet (FUV) and near-ultraviolet (NUV) observations from the *Galaxy Evolution Explorer* (*GALEX*, Martin et al. 2005; Morrissey et al. 2007). Most of our galaxies were observed through our Cycle 3 program (GI3-089), but six are from archival images. *GALEX* acquires images in FUV ($1344 - 1786$Å) with a $4.3''$ FWHM PSF, and in NUV ($1771 - 2831$Å) with a $5.3''$ FWHM PSF. The images are processed and calibrated with the standard pipeline and were downloaded from the archive. The fluxes are measured in large apertures on the calibrated images. These UV images are especially sensitive to recent star formation, and provide a critical measurement of the presence and impact of young stars in the BCDs.

Some of our optical photometry comes from Sudarsky (1995) and Norton (1997), which contain complete details of their reduction and calibration. In brief, the UBVRI optical CCD observations were carried out at the Kitt Peak National Observatory[5] (KPNO) 0.9m telescope in November/December 1989 and April 1990. The images were calibrated with observations of Landolt standards, and total fluxes were measured. NIR JHK photometry was also obtained at KPNO with IR arrays (Salzer & Elston 1992). Table 1 shows which photometric measurements come from this dataset (labeled "SN"), and the fluxes are given in Table 2.

We have expanded this existing optical/NIR photometry with new observations from the WIYN[6] 3.5-m telescope at KPNO. Complete details of the observations, reductions, and calibrations are given in Janowiecki & Salzer (2014). In short, the Minimosaic and OPTIC (Orthogonal Parallel Transfer Imaging Camera) imagers were used to obtain optical observations and the WHIRC (WIYN High Resolution Infrared Camera, Meixner et al. 2010) imager was used to obtain NIR observations. Observations were taken between November 2008 and April 2010, and were calibrated with catalog measurements from Sloan Digital Sky Survey (SDSS)

[5] Kitt Peak National Observatory, National Optical Astronomy Observatory, which is operated by the Association of Universities for Research in Astronomy (AURA) under cooperative agreement with the National Science Foundation.

[6] The WIYN Observatory is a joint facility of the University of Wisconsin-Madison, Indiana University, the University of Missouri, and the National Optical Astronomy Observatory.

TABLE 2
OBSERVED FLUXES OF THE BCD SAMPLE

Galaxy	f_{FUV} σ_{FUV} [mJy]	f_{NUV} σ_{NUV} [mJy]	f_U σ_U [mJy]	f_B σ_B [mJy]	f_V σ_V [mJy]	f_R σ_R [mJy]	f_I σ_I [mJy]	f_J σ_J [mJy]	f_H σ_H [mJy]	f_{K_s} σ_{K_s} [mJy]	$f_{3.6\mu}$ $\sigma_{3.6\mu}$ [mJy]	$f_{4.5\mu}$ $\sigma_{4.5\mu}$ [mJy]	$f_{5.8\mu}$ $\sigma_{5.8\mu}$ [mJy]	$f_{8.0\mu}$ $\sigma_{8.0\mu}$ [mJy]	$f_{24\mu}$ $\sigma_{24\mu}$ [mJy]	$f_{70\mu}$ $\sigma_{70\mu}$ [mJy]	$f_{160\mu}$ $\sigma_{160\mu}$ [mJy]
UM 323	0.712	0.700	···	1.445	1.540	1.670	1.864	2.638	2.338	1.900	···	···	···	···	···	···	···
	···	0.001	···	0.013	0.040	0.062	0.017	0.165	0.125	0.258	···	···	···	···	···	···	···
UM 408	0.153	0.179	···	0.361	0.420	0.437	0.484	0.492	0.472	···	···	···	···	···	···	···	···
	0.003	0.002	···	0.003	0.037	0.039	0.008	0.040	0.031	···	···	···	···	···	···	···	···
Mk 600	0.792	0.924	···	2.524	2.788	3.051	3.296	3.978	3.985	2.647	2.083	1.879	1.680	1.440	21.568	161.2	139.6
	0.005	0.004	···	0.026	0.226	0.248	0.024	0.161	0.143	0.217	0.250	0.238	0.237	0.208	1.716	9.4	20.2
II Zw 40	0.086	0.091	1.028	2.034	3.336	6.241	9.719	20.722	23.902	20.627	24.962	23.463	54.652	134.6	1616	4787	1427
	0.005	···	0.044	0.058	0.092	0.161	0.242	0.534	0.815	0.494	0.903	0.869	1.391	2.1	15	48	109
Mk 5	0.308	0.410	0.946	1.550	1.902	2.984	3.198	3.509	3.802	2.742	···	6.745	···	19.041	16.118	236.8	144.7
	0.004	0.003	0.044	0.033	0.070	0.259	0.027	0.239	0.210	0.202	···	0.462	···	0.790	1.459	10.0	17.0
CG 10	0.141	0.153	···	0.281	0.433	0.458	···	0.422	0.504	0.355	···	···	···	···	···	···	···
	0.003	0.002	···	0.014	0.035	0.038	···	0.019	0.033	0.033	···	···	···	···	···	···	···
I Zw 18	1.293	1.176	0.881	0.905	0.795	0.731	0.649	0.601	0.452	0.565	···	···	···	···	5.827	36.058	···
	0.010	0.006	0.043	0.022	0.018	0.017	0.019	0.037	0.041	0.085	···	···	···	···	0.863	4.595	···
Was 5	0.247	0.299	0.322	0.501	0.685	0.814	···	0.986	0.786	0.667	···	···	···	···	···	···	···
	0.004	0.003	0.013	0.014	0.019	0.011	···	0.054	0.072	0.096	···	···	···	···	···	···	···
Mk 36	1.590	1.574	1.615	1.893	1.808	2.432	···	2.643	2.312	1.937	···	1.165	···	1.645	26.197	368.0	51.638
	0.012	0.007	0.062	0.052	0.048	0.031	···	0.122	0.143	0.148	···	0.182	···	0.224	1.950	15.9	9.159
UM 439	1.482	1.779	2.188	3.251	3.449	3.628	···	4.752	4.357	2.858	···	···	···	···	···	···	···
	0.013	0.006	0.103	0.096	0.099	0.043	···	0.149	0.133	0.155	···	···	···	···	···	···	···
Mk 750	···	···	1.603	2.235	2.687	3.108	···	3.054	2.938	2.968	···	···	···	···	···	···	···
	···	···	0.069	0.066	0.074	0.040	···	0.107	0.152	0.159	···	···	···	···	···	···	···
UM 461	0.462	0.534	0.618	0.974	1.052	1.251	···	1.328	1.205	0.637	0.787	0.625	0.826	1.659	34.178	272.1	···
	0.010	0.007	0.031	0.033	0.037	0.016	···	0.067	0.087	0.118	0.148	0.130	0.160	0.225	2.164	16.3	···
UM 462	2.832	3.232	3.480	4.529	4.622	5.629	···	5.572	4.840	3.163	3.452	3.262	4.943	8.185	115.9	866.6	278.1
	0.022	0.016	0.215	0.163	0.170	0.067	···	0.205	0.147	0.175	0.327	0.317	0.439	0.546	4.0	19.7	21.9
Mk 67	0.237	0.371	0.767	1.064	1.293	1.565	1.800	2.268	1.988	1.247	···	···	···	···	···	···	···
	0.004	0.003	0.035	0.027	0.032	0.039	0.051	0.094	0.099	0.113	···	···	···	···	···	···	···
Mk 475	0.318	0.436	0.687	0.992	1.292	1.452	···	1.883	1.698	1.297	1.029	0.811	0.751	0.950	10.571	117.3	···
	0.011	0.003	0.027	0.028	0.035	0.019	···	0.094	0.097	0.098	0.171	0.151	0.148	0.167	1.167	7.5	···
Mk 900	0.715	1.101	···	4.613	8.318	10.745	12.394	16.384	17.475	12.707	10.060	6.775	10.556	19.652	···	417.9	380.6
	0.005	0.005	···	0.081	0.261	0.485	0.069	0.498	0.515	0.421	0.567	0.464	0.586	0.798	···	14.4	25.4
Mk 324	0.700	0.818	1.514	2.780	3.726	5.321	5.167	6.874	7.593	5.593	···	···	···	···	···	···	···
	0.008	0.005	0.056	0.013	0.103	0.147	0.024	0.215	0.224	0.191	···	···	···	···	···	···	···
Mk 328	0.324	0.435	1.213	2.542	3.938	6.457	6.843	10.765	12.463	8.938	···	···	···	···	···	···	···
	0.004	0.003	0.045	0.028	0.109	0.178	0.032	0.317	0.230	0.181	···	···	···	···	···	···	···

NOTE. — Fluxes come from directly from sources listed in Table 1; when multiple observations in the same filter exist, we use the one with the lowest uncertainty. No Galactic extinction corrections have been applied, and no minimum error floors have been enforced to these fluxes. *GALEX* fluxes without pipeline-determined uncertainties are assigned errors of 5%.

TABLE 3
Hα observations and abundances of the BCDs

Galaxy (1)	Hα luminosity $\times 10^{39}$ [erg/s] (2)	Distance [Mpc] (3)	Z 12+log(O/H) (4)
UM 323	38.5	25.6	7.96[a]
UM 408	35.2	47.5	7.74[a]
Mk 600	27.3	13.6	7.94[a]
II Zw 40	40.3	11.1	8.09[a]
Mk 5	7.7	15.3	8.06[a]
CG 10	···	30.7	···
I Zw 18	24.3	18.2	7.18[a]
Was 5	14.3	23.1	7.85[b]
Mk 36	6.8	8.4	7.82[a]
UM 439	16.2	15.9	8.08[a]
Mk 750	2.7	5.2	8.18[b]
UM 461	9.1	12.7	7.81[c]
UM 462	32.6	13.5	7.80[c]
Mk 67	17.4	18.7	8.08[a]
Mk 475	6.9	11.9	7.93[a]
Mk 900	84.0	18.9	8.07[a]
Mk 324	31.3	23.2	8.18[d]
Mk 328	23.8	20.6	8.64[d]

Note. — Column 3: distances from NED. Column 4: gas phase abundance $Z = 12+\log(O/H)$. Sources of abundances are: [a] T_e abundances from Zhao et al. 2010; [b] N2 abundance from Zhao et al. 2010; [c] Brinchmann et al. 2008; [d] Izotov et al. 2007;

and Two Micron All Sky Survey (2MASS) of stars in the fields with our targets. Table 1 shows which flux measurements come from our recent WIYN observations (labeled "W"), and our complete set of fluxes and uncertainties are reported in Table 2.

We also have calibrated narrow band Ha observations of the BCD sample which are used to determine SFRs from the standard prescription of Kennicutt (1998). These Hα fluxes were measured from narrow-band imaging (Salzer & Elston 1992), and the calibrated Hα luminosities are given in Table 3, along with metallicity values from the literature for the BCD sample. Distances in Table 3 use flow models (Virgo+GA+Shapley) from the NASA Extragalactic Database (NED[7]), and for I Zw 18 we use the tip of the red giant branch distance from Aloisi et al. (2007).

2.2. *Observations of the LVL sample*

The multi-wavelength observational data of the 258 galaxies in the LVL sample are nearly identical in quality and wavelength coverage to our observations of the BCD sample. The SEDs for the complete LVL sample are presented in Cook et al. (2014b). These SEDs include *GALEX* FUV and NUV images (Lee et al. 2011), ground-based optical UBVRI images (Cook et al. 2014a), NIR JHK images from 2MASS (Two Micron All Sky Survey Dale et al. 2009), and Spitzer IR images (Dale et al. 2009). This observational dataset is used to determine the multi-wavelength SEDs from

[7] This research has made use of the NASA/IPAC Extragalactic Database (NED) which is operated by the Jet Propulsion Laboratory, California Institute of Technology, under contract with the National Aeronautics and Space Administration.

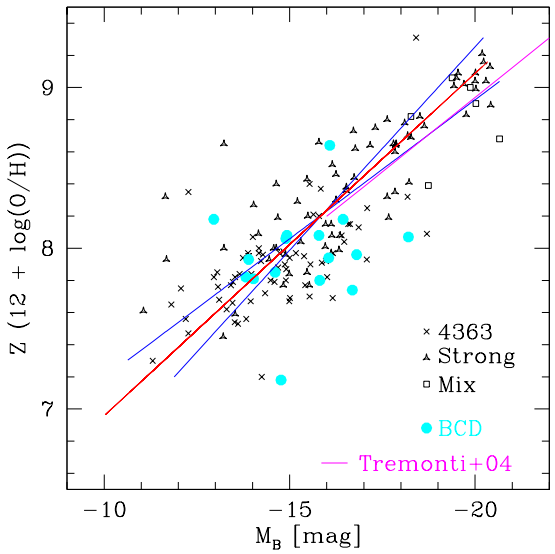

Fig. 1.— Different symbols show the L-Z relation for all of the LVL galaxies with measured gas-phase metallicities (various methods). The solid blue lines show the best forward-fit and reverse-fit to this relationship, and the red line shows their average. Members of our BCD sample are shown as blue points at their measured abundances. The magenta line shows the best-fit L-Z relation from Tremonti et al. (2004), which agrees well with our fit.

1500Å−24μm for galaxies in the LVL sample. Constructing SEDs with self-consistent UV, optical, NIR, and FIR fluxes is a complex process, and care was taken to measure the galaxies within a common aperture across all wavelengths (Cook et al. 2014b). In all, fluxes are reported in 14 band-passes between *GALEX* FUV and Spitzer 24μm for all of the 258 LVL galaxies. As noted by Cook et al. (2014b), there are 47 upper limits on non-detections in the IR observations, 13 upper limits in the UV observations, and 1 upper limit in the optical data. In total, 3551 fluxes are used in the LVL SEDs. Cook et al. (2014b) present the LVL SEDs and derive physical properties from them, including their star formation rates, stellar masses, and internal extinction

In addition to the complete set of panchromatic SEDs, gas-phase metallicities have been measured for much of the LVL sample. Cook et al. (2014b) compiles metallicity measurements from Marble et al. (2010), Berg et al. (2012), and Moustakas et al. (2010), which come from different metallicity methods calibrations (see Marble et al. 2010; McGaugh 1991; Pilyugin & Thuan 2005; Kobulnicky & Kewley 2004). Of the 258 galaxies in LVL, 155 have measured metallicities (about half "direct" and half "strong-line" methods), which are shown in the luminosity-metallicity relationship (L-Z) in Figure 1. Also shown in Figure 1 is the L-Z relation from Tremonti et al. (2004) for a sample of $\sim$53,000 SDSS galaxies brighter than M_B=−16 mag, which agrees well with the L-Z relation from the LVL and BCD samples.

2.3. *BCDs in LVL*

Some of the galaxies in LVL have been classified as BCDs – in particular Mk 475 is a member of both our BCD sample and of the LVL sample. For brevity, throughout this work we refer to the "BCD sample" and the "LVL sample", but there exists a continuum of galaxy properties across both samples. The LVL sam-

ple (Dale et al. 2009) includes both early- and late-type galaxies, and in particular includes 7 objects which identified as BCDs in the Palomar/Las Campanas Atlas of BCDs (Gil de Paz et al. 2003; Kennicutt et al. 2008).

On subsequent plots and figures we take care to indicate these individual populations (BCD, irregular/spiral, early-type) within the LVL sample. Our goal is not to demarcate BCDs from "normal" dwarf galaxies, but rather to explore the extremes of dwarf galaxy evolution. BCDs are often characterized by their significant star formation rates, but they are unique in other aspects as well. Throughout this work we will discuss the continuum of dwarf galaxy properties, and show the extreme position that BCDs occupy.

2.4. *SEDs*

Figure 2 shows the complete set of observed SEDs for our sample of BCDs. The SEDs have been corrected for Galactic extinction (via Schlegel et al. 1998, for consistency with the LVL photometry) and are shown in flux units of mJy. Also shown are $100'' \times 100''$ color cutout images from SDSS Data Release 12 (DR12, Alam et al. 2015), where available. The SEDs shown in Figure 2 demonstrate the amount and quality of the photometric observations of this sample. Most of the BCDs have UV fluxes, and many have complete Spitzer FIR coverage as well. When compared with the average SEDs of the low-mass late-type (non-BCD) LVL galaxies (e.g., Figure 5 of Cook et al. 2014b, , and shown in our Figure 2), the BCDs show much flatter (bluer) SEDs at UV/optical wavelengths. This is consistent with the presence of substantial recent star formation activity. The three most massive galaxies in our sample (Mk 324, Mk 328, Mk 475, Mk 900) have noticeably redder optical SEDs, and also have smooth elliptical isophotes in their outskirts. These three galaxies are classified as BCD type "nE" by Gil de Paz et al. (2003), and will be referred to as "BCD/E" on subsequent plots.

Across the sample of BCDs, the UV slope shows significant variations from the steep rise of Mk 67 to the flat slope of Mk 36. The UV slope is sensitive to both the internal absorption from dust as well as the current star formation. The IR observations are necessary to disentangle the effects of dust and star formation.

The detailed shapes of these panchromatic SEDs encode much of the information about the star formation history, stellar populations, and dust in the BCD sample. The SEDs of each LVL galaxy are not reproduced here, but are shown and discussed extensively in Cook et al. (2014b).

3. FITTING SEDS

We fit our SEDs with CIGALE (Code Investigating Galaxy Emission, Noll et al. 2009). CIGALE fits SEDs from UV to far infrared in order to account for dust absorption and re-emission in a self-consistent manner. It creates a grid of synthetic SEDs based on theoretical models to account for all of the relevant line and continuum emission and absorption from stars, gas, and dust. This grid of models is then compared with observed SEDs in order to determine the most likely values and uncertainties for various physical parameters. In the following sub-sections we describe the models that CIGALE uses to generate SEDs, our verifications of the appropriateness of the models, and the consistency checks we employ to understand the reliability of the fit results.

3.1. *Input Models*

CIGALE uses theoretical models to parametrize the flux emitted and absorbed by the stars, gas, and dust in model galaxies, and produces a grid of model spectra which are then converted to SEDs. Noll et al. (2009) describes the input models in complete detail, and we briefly review each component and its contribution.

The stellar emission is modeled using stellar population synthesis models from Bruzual & Charlot (2003) with a Salpeter IMF, between metallicities of Z=0.0001 and Z=0.05. Two stellar populations are typically used: young and old stellar populations. The light from the stellar populations represents the dominant source of emission in the UV-optical range.

Nebular line and continuum emission are included in the UV-NIR range, taking into account escape fraction and dust absorption. Using the number of Lyman continuum photons (from the stellar continuum) to compute the strength of the Hβ line, a metallicity-dependent template is used to determine the strengths of 119 other nebular lines via an estimate of the number of ionizing photons (Inoue 2011).

Dust attenuation is handled with the formulas from Calzetti et al. (2000) and Leitherer et al. (2002), based on the method of Cardelli et al. (1989). In general, this requires computing and applying the attenuation curve (A(λ)/E(B−V)) to all of the relevant flux-emitting components considered in the model (both stellar and nebular emission). The Calzetti et al. (2000) attenuation law is used as a baseline but we allow its slope to change by multiplying it by $(\lambda/\lambda_{\rm V})^{\delta}$ where $\lambda_{\rm V}$ = 5500Å, and δ ranges between −1 and 2.5. This modification is required based on the variations seen in the (limited number) of observations of the extinction law in other galaxies (Witt & Gordon 2000; Inoue et al. 2006). The attenuation is combined with the emission models as a "negative" flux, and is calculated separately for each component of the model. The attenuation applied to the light coming from the old stellar population is reduced by a factor of $f_{\rm att}$ = 0.5 from the value of the young population, to account for the dustier nature of star forming regions. This has a small effect.

A key advantage of CIGALE's SED-fitting is its multi-wavelength energy balance, and that consideration drives its treatment of infrared re-emission from heated dust. CIGALE combines the amount of attenuation present in the models with the semi-empirical re-emission templates of Dale et al. (2014). The templates are generated by considering the contributions from a variety of dust heating intensities and depend on a single heating parameter, α. This exponent is the only free parameter in the dust re-emission models as the total energy is constrained to be equivalent to the amount that has been attenuated. CIGALE is also capable of modelling the emission from a dust-enshrouded AGN, but we do not include that option in our fits; BCDs do not host AGN, and LVL contains mostly late-type dwarf galaxies (NGC 855 is the most massive elliptical galaxy in sample, at only $\sim 10^9 M_{\odot}$), so we do not expect any significant AGN emission.

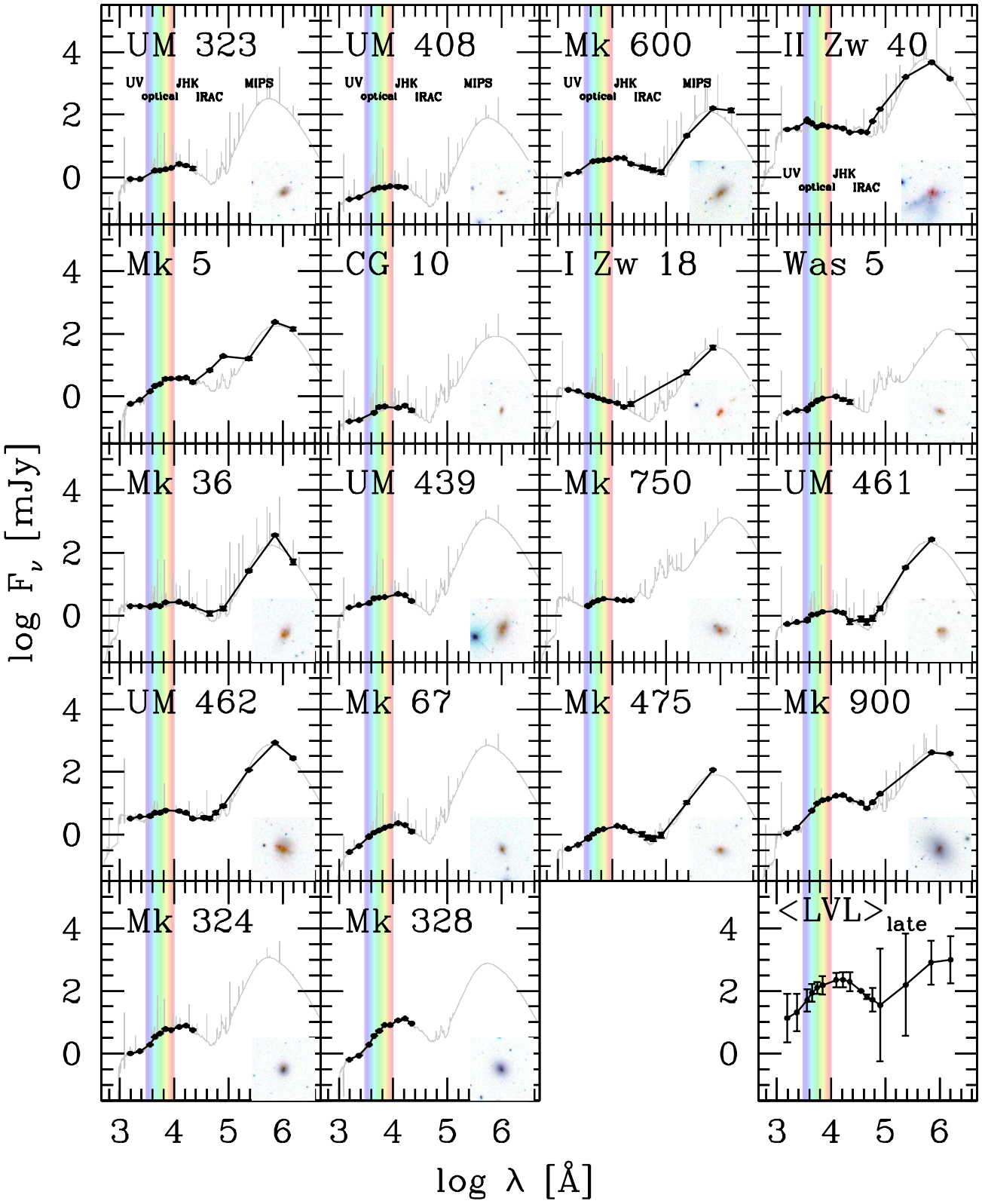

FIG. 2.— All SEDs for our BCD samples. In each panel, the flux density (in mJy) in each filter is shown by a dot at that filter's effective wavelength. The photometric uncertainties are shown as error bars on the flux points, but are nearly always smaller than the points. Color thumbnails $100'' \times 100''$ from SDSS are shown in inverse video on each panel, where available. An average SED for late-type low-mass LVL galaxies is shown in the bottom right panel. It includes 92 LVL galaxies (none classified as BCDs) with stellar mass $< 10^9 M_\odot$, with measured fluxes in all filters, normalized to $F_{3.6\mu} = 100$ mJy, and with error bars showing standard deviations at each wavelength. Light grey lines show the full spectra from the best-fitting SED models for each BCD.

CIGALE computes and applies the attenuation resulting from the effects of the intergalactic medium (IGM), based on the prescription of Meiksin (2006). While this attenuation is relatively small for the nearby galaxies, we include it for consistency when comparing with galaxies at different redshifts. The contribution of the IGM to the overall attenuation is most relevant at very short wavelengths.

We can consider a wide variety of SFH scenarios in our models. CIGALE currently includes three standard options: A double decreasing exponential model, a "delayed" model, and a manually created SFH supplied by the user. We primarily consider the double exponential model, which describes the SFH as two exponential functions characterized by e-folding time τ. The age and τ of both populations are free parameters, as is the mass fraction of the young population compared to the old population. A minimum age separation can be enforced between the two populations, and is typically set at 10 Myr. In the following sub-sections, we consider increasingly complex SFH assumptions and the results of the SED fits.

3.2. *Preliminary SED-fitting tests*

To gain familiarity and confidence in the SED fitting methods and results, we first considered simple SFH scenarios with very few free parameters (e.g., a single recent burst on top of an old burst, or on top of a constantly star-forming population). We varied grid parameters, sampling densities, and explored the effects these choices had on the outputs of the SED fits. Full details and results of these extensive tests can be found in Chapter 3 of Janowiecki (2015). In brief, we used a variety of diagnostics to check that the SED fits were reasonable, and also to realistically assess the quality of the outputs. In the following sub-sections, we discuss the grid choices and quality assessments of the fits and their results.

3.3. *SFH and grid parameters*

In order to characterize a stellar population a SFH must be assumed. We use CIGALE's double-exponential option to create a two-population SFH. Both the old and young stellar populations are described by declining SFRs which began abruptly and exponentially decline. In these fits, both the age and exponential scale time are allowed to vary, with the sampling of possible values shown in Table 4. Note that while the old stellar population age is allowed to be as young as 1000 Myr and the young stellar population is allowed to be as old as 3000 Myr, we require $\mathrm{age}_o > \mathrm{age}_y + 10$ Myr, to keep a meaningful distinction between the old and young stellar populations.

In this grid, the mass fraction of the young population is allowed to vary between 1% and 50%. The dust attenuation, E(B−V), varies from 0.01 to 1.5 magnitudes, the Calzetti law is modified by a power law slope between −1 and 2.5, and the dust heating parameter α varies between 0.5 and 2.5. The stellar metallicity is a free parameter and varies between $Z = 0.0001$ and 0.05. See Section 3.1 for further details on these parameters.

This grid requires $\sim$1,000,000 SEDs to be computed, and the process of generating and fitting the SEDs takes about an hour on a laptop computer. Once the entire library of SEDs for each grid point is generated, they can be compared with our observed SEDs. Before carrying out the actual fitting process, we first demonstrate that the model grids are suitably well-matched and appropriate for fitting our observed SEDs.

Following the method described in Section 3.2 of Buat et al. (2011), we test whether the colors of the model grids sufficiently overlap with our observed SEDs by placing them onto diagnostic color-color diagrams. We consider the FUV−NUV and NUV−R colors because of their connections with dust attenuation and star formation history. We also show the FUV−70μ color for its very large wavelength baseline, and the B−V and B−H colors as they are commonly used. Figure 3 shows these diagnostic color-color plots. The galaxy with the most extreme FUV-NUV color is KDG 061, a tidal dwarf galaxy in the M81 group. Its *GALEX* observations are very deep (16,238s exposure time), but its FUV flux is very weak. Its optical colors are typical of dSphs but it has significant amounts of HI and Hα emission indicating ongoing star formation (Johnson et al. 1997; Croxall et al. 2009).

Figure 3 also demonstrates the correlations between these colors in the models. Models are selected from within a single shaded pixel on the left panel (shown in green) and plotted on the other two plots at their appropriate colors. Similarly, models are selected from a single pixel on the right panel (in blue) and are shown on the other two diagrams. These model points demonstrate the connections between the different color-spaces, and the strengths of multi-wavelength SEDs from UV to IR.

Overall, it is clear that our model grids are sampling an adequate amount of color-color space to match most of the observations. Our choice of parameters for the stellar populations and dust attenuation appear to cover an appropriate range of values to be useful in fitting our observations.

3.4. *Fitting SEDs and determining output values*

Now that we have shown that the colors of our model grids are suitable comparisons to our observations, we can proceed to fit the SEDs. To determine the best-fit values of each parameter for each observed SED, CIGALE first calculates the χ^2 value between the observations and each model grid point SED. As described by Equation (5) from Noll et al. (2009), this is calculated using:

$$\chi^2(M_{\mathrm{gal}}) = \Sigma_{i=1}^{k} \frac{(M_{\mathrm{gal}} f_{\mathrm{mod},i} - f_{\mathrm{obs},i})^2}{\sigma^2_{\mathrm{obs},i}} \qquad (1)$$

where the difference between each flux measurement ($f_{\mathrm{obs},i}$) and each model flux point ($f_{\mathrm{mod},i}$) is divided by the uncertainty on the observed flux ($\sigma^2_{\mathrm{obs},i}$), in filter i (see also Salim et al. 2007). The model fluxes are given per unit $\mathrm{M}_\odot$, so are multiplied by the galaxy mass ($\mathrm{M}_{\mathrm{gal}}$). This summation is taken over all flux observations (k) in the SED. The photometric uncertainties on the flux observations, σ_{obs}, are included as a weighting factor.

After determining values of χ^2 between a galaxy's SED and all of the model grid points, CIGALE generates probability distribution functions (PDFs) for selected parameters in a Bayesian-like framework (Kauffmann et al. 2003; Salim et al. 2005, 2007; Noll et al. 2009). For each parameter, CIGALE creates a number of bins between

TABLE 4
INPUT PARAMETERS FOR SED MODEL GRID

Parameter	Symbol	Values	Units
Old stellar population age	age_o	1000, 3000, 10000	Myr
Old stellar population e-folding time	τ_o	100, 1000, 10000	Myr
Young stellar population age	age_y	30, 100, 300, 1000, 3000	Myr
Young stellar population e-folding time	τ_y	10, 100, 1000	Myr
Young stellar population mass fraction	f_b	0.01, 0.03, 0.1, 0.3, 0.5	···
Stellar metallicity	Z	0.0001, 0.0004, 0.004, 0.008, 0.02, 0.05	$Z/Z_\odot$
Amount of dust attenuation	$\mathrm{E(B-V)}_y$	0.01, 0.02, 0.05, 0.1, 0.2, 0.3, 0.4, 0.5, 1	mag
Power-law slope on extinction law	δ	$-1, -0.5, 0, 0.5, 1, 1.5, 2, 2.5$	···
Dust heating parameter	α	0.5, 1, 1.5, 2.5	···

NOTE. — Note that we require $\mathrm{age}_o > \mathrm{age}_y + 10$ Myr, to enforce a separation between the old and young stellar populations.

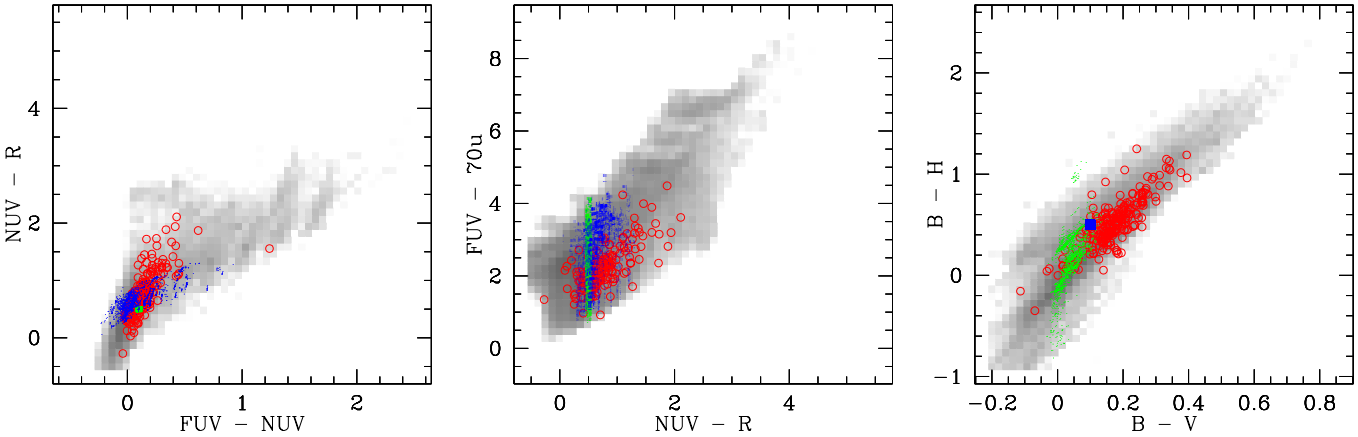

FIG. 3.— Shaded grey cells indicate the number density of grid points in that cell. Red circles indicate the observed colors of our BCD sample and LVL galaxies. Small green points show grid points within a single pixel bin on the left panel and their corresponding colors on the other panels. Small blue points are selected in a single pixel bin from right panel.

its lowest to highest values, and determines which models fall into each bin for that parameter. Among the models in each bin, the model with the highest probability (i.e., best match to observed SED) is found and reported. With these maximum probabilities from each bin, a PDF can be generated which represents the maximum envelope of the probability distribution for that parameter. These PDFs are used to generate expectation values and uncertainties (see Figures 6 and 7 in Noll et al. (2009) for further details about this method). The key analyzed parameters from the fits are described in Table 5, their error determinations are discussed further in Section 3.5, and the best-fit values for the BCD sample are shown in Table 6.

We use CIGALE to fit SEDs using all of the fluxes from UV (FUV/NUV), optical (UBVRI), near-infrared (JHK), and infrared (Spitzer IRAC-MIPS). We examine the distribution of reduced χ^2 values from the best-fitting SEDs to assess the success at fitting our observations. Figure 4 shows the reduced χ^2 distribution for our fits. On average, the reduced χ^2 is 1.97, and only 11 galaxies have $\chi^2 > 5$.

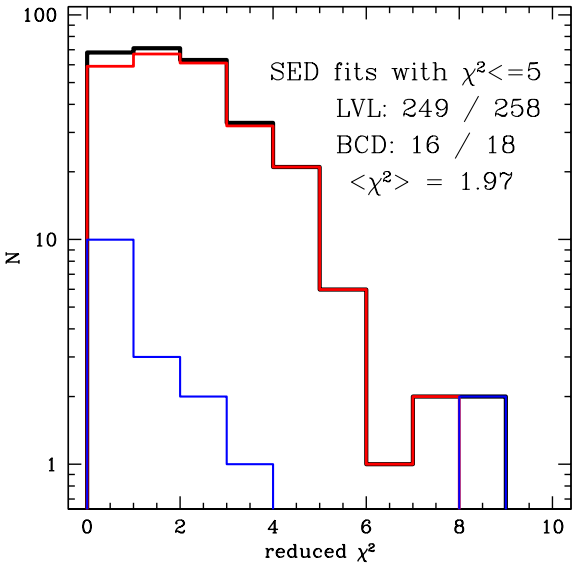

FIG. 4.— Distributions of values of reduced χ^2 from our SED fits. The thick black line shows the distribution of the combined LVL and BCD samples, while the BCDs are shown separately in blue and the LVL galaxies are shown separately in red.

3.5. *Reliability and uncertainty estimates*

We now describe a few verifications and consistency checks which were used to estimate the reliability and uncertainty of the SED fits.

It is important to verify that the parameter space covered by the grid is of suitable resolution and range. Inadequate resolution in a particular parameter will decrease the accuracy of that parameter's determination, while over-sampling a poorly constrained parameter can arti-

TABLE 5
KEY ANALYZED PARAMETERS FROM SED FITS

Parameter	Description	units
$\langle SFR \rangle_{10}$	SFR averaged over 10 Myr	$M_\odot$/yr
$\langle SFR \rangle_{50}$	SFR averaged over 50 Myr	$M_\odot$/yr
$\langle SFR \rangle_{100}$	SFR averaged over 100 Myr	$M_\odot$/yr
$\langle SFR \rangle_{500}$	SFR averaged over 500 Myr	$M_\odot$/yr
$\langle SFR \rangle_{1000}$	SFR averaged over 1000 Myr	$M_\odot$/yr
$\langle SFR \rangle_{all}$	SFR averaged over lifetime	$M_\odot$/yr
$M_{\star,o}$	Stellar mass of old stellar population	$M_\odot$
$M_{\star,y}$	Stellar mass of young stellar population	$M_\odot$

NOTE. — All input parameters are also analyzed.

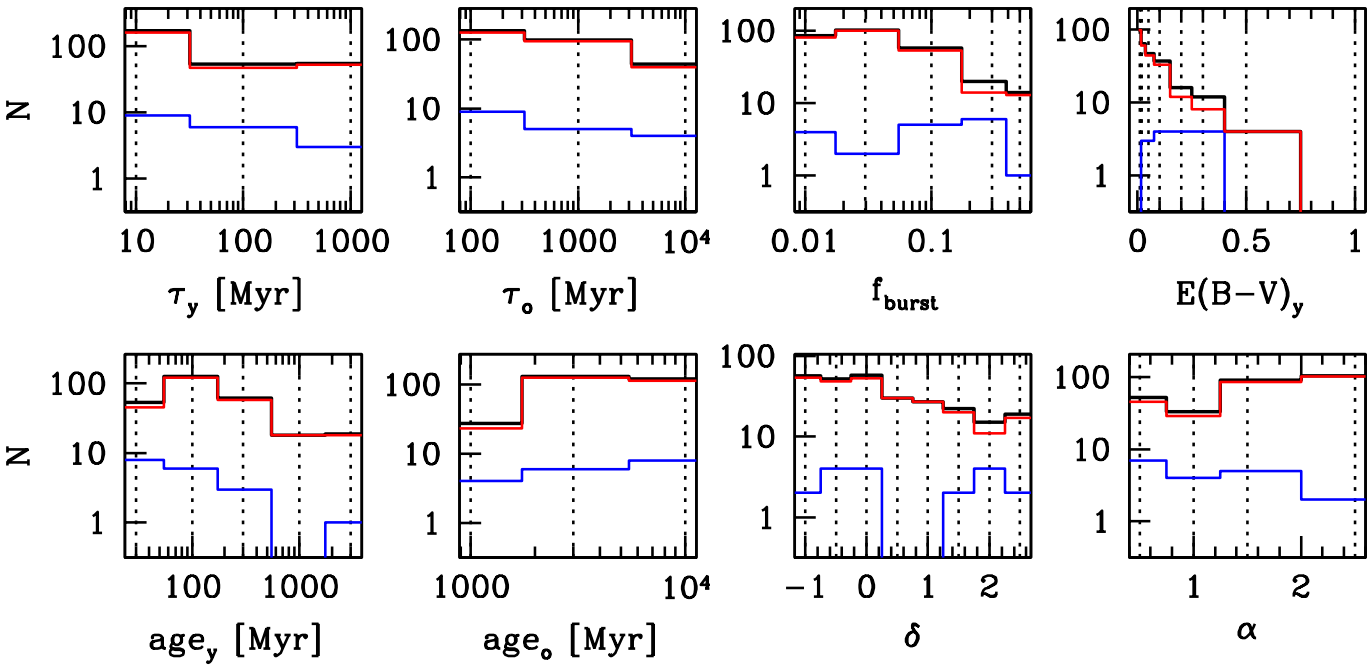

FIG. 5.— Sample of parameter distributions. Vertical dotted lines show grid points. Histograms of the best-fit results are shown in black for the complete sample, in red for the LVL sample, and in blue for the BCD sample.

ficially increase its uncertainty or negatively impact the determinations of other parameters (Buat et al. 2011). Figure 5 shows histograms of the best-fitting results for the most relevant parameters.

We experimented with different ranges and resolution of these parameters until satisfactory distributions were obtained. Initially, our grid was too narrow and some of the histograms showed unrealistically narrow spikes at the extremes of parameter space. We expanded the range of parameter space (by expanding the maximum or minimum values of the parameters) until there were no unrealistic peaks at the edges. Many of the parameters are logarithmically sampled in order to smoothly cover the wide range of parameter space. The resolution in each parameter was also adjusted until a generally smooth and continuous histogram was obtained, to eliminate unrealistically sharp features which were artifacts of inadequate sampling. The practical constraints of computing time were also considered, which prevented the grids from becoming unmanageably large. The resulting grid represents a compromise between covering the necessary parameter space with enough resolution and restricting the computational needs within reason. The final choices for parameter sampling are shown in Table 4.

In order to estimate the reliability of the SED fit results for each galaxy, we start with the best-fitting grid point for each object. This best-fitting model SED is treated as a "mock" observation (retaining the original photometric uncertainties on the real observations), and re-fitted with the same grid to re-generate the most likely value of each parameter. This "mock" fitting method allows us to estimate the reliability of the SED fit results (Salim et al. 2009; Giovannoli et al. 2010) by comparing "known" input parameters of the model SED with its re-fitted parameters.

Figure 6 shows shows the results of our mock analysis for nine of the analyzed parameters. As before, we only show the SED fits which have a reduced $\chi^2 < 5$ and which had a complete set of observations for all 15 flux points. Shown on the x-axes are the exact values of each parameter used to generate the "mock" SEDs. The y-axes show the differences between the exact "mock" values and the best-fit values from the SED re-fitting

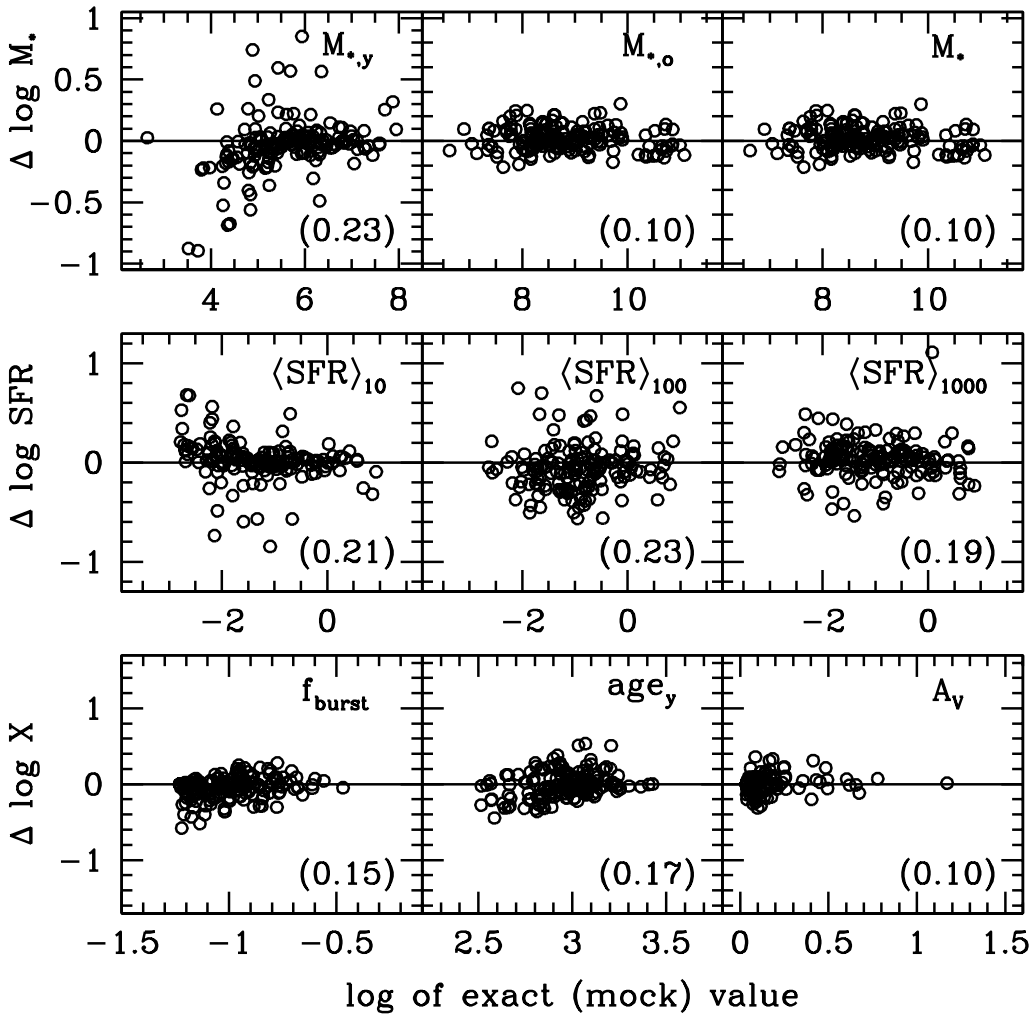

FIG. 6.— Results from mock analysis for the combined BCD and LVL samples. For each of these nine selected parameters, the x-axis shows the exact ("mock") value while the y-axis shows the difference between the exact and re-fitted value. The top row shows the mass estimates for the young, old, and total stellar populations, in units of solar masses. The middle row shows three SFR estimates, averaged over 10, 100, and 1000 Myr, all in units of solar masses per year. The bottom row shows the logarithmic differences for "X", where X in the first column is the mass fraction of the burst population, in the second column is the age of the burst population (in Myr), and in the third column is the dust attenuation (A_V, in magnitudes). In all panels, the number in parentheses indicates the standard deviation of the distribution of points shown.

process. The number in parentheses at the bottom right corner of all panels is the rms scatter for that parameter.

In some cases, the exact parameter values in the "mock" SEDs can be reliability recovered by our fits. For example, the mass of the old stellar population ($M_{\rm o,stellar}$) shows no systematic trends and a scatter of only 0.10 dex. However, the mass of the young stellar population ($M_{\rm y,stellar}$) has more scatter and perhaps a slope or offset at the lowest stellar masses. Furthermore, the best-fit values of the age of the young stellar population ($\rm age_y$) show a small systematic trend where younger ages are likely to be under-estimated and older ages are likely to be over-estimated.

The reliability of these parameters varies in this mock analysis, but these reliability estimates are only useful in conjunction with χ^2 indicators and other independent verifications of the SED fits. The deviations shown here represent the reliability of the fit results, independent from our actual observations. The differences in best-fit parameters of the mock SEDs and the re-fit SEDs give an estimate of the reliability of this grid and method, and show which parameters are more reliably determined in this type of analysis. Some parameters are more reliably fit than others (e.g., the stellar mass of the young population has a great scatter than the stellar mass of the old population), which is incorporated into the uncertainties listed in the error budget in Table 7. This error budget also includes the full Bayesian uncertainties generated from our fitting procedure.

3.6. *Further verifications*

In addition to these internal consistency checks on the SED grids and fitting methods, we can also use comparisons with independent determinations of similar parameters to verify our results. Most importantly, we can compare our SED-derived SFRs with those determined from Hα observations. We can also compare the SED-derived SFRs with estimates from the UV flux and compare the SED-derived stellar masses with estimates from 3.6μm flux and $\rm K_s$ flux. These are less independent comparisons than in Hα as these fluxes are already included

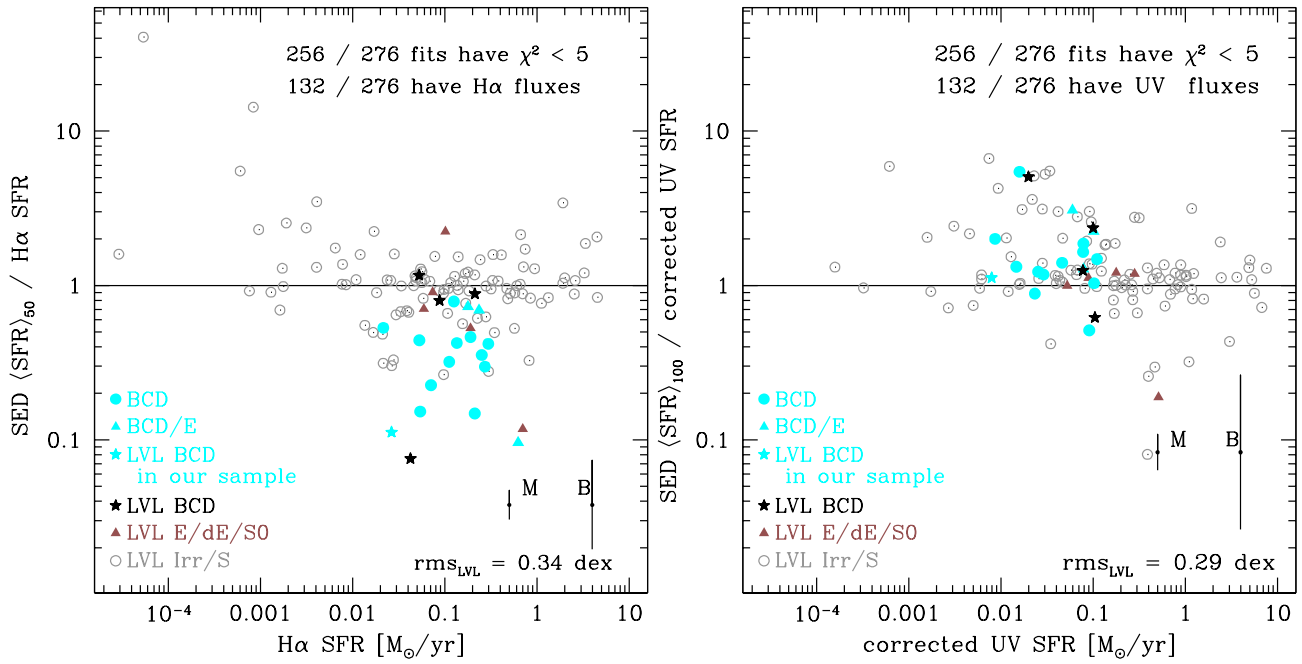

FIG. 7.— SFR comparisons between SED fits, Hα , and UV observations. Galaxies are plotted by morphology; LVL irregulars/spirals are grey circles, LVL E/dE/S0 are red triangles, LVL BCDs are black stars, and Mk 475 is shown as a cyan star. Our BCD sample is plotted as cyan dots, with the nE BCDs shown as cyan triangles. The left panel compares the 50-Myr average SED SFR and the Hα SFR. The right panel compares the 100-Myr average SED SFR and the SFR from the extinction-corrected UV luminosity (which is also included in the SED fit). The RMS scatter is measured for late-type LVL galaxies only. The representative error bars at the bottom right of both panels show the average deviations from the mock method ("M") and the average Bayesian uncertainty ("B").

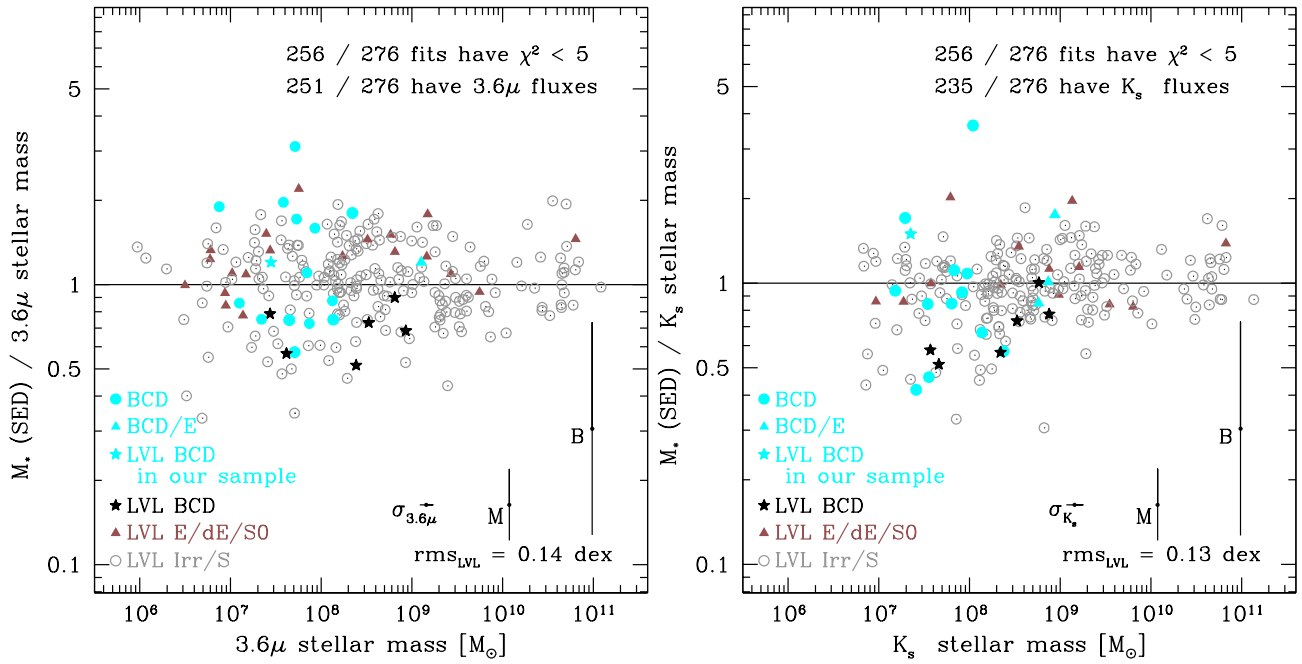

FIG. 8.— Stellar mass comparisons between SED fits and simple M/L estimates, with the same color-coding as Figure 7. The left panel compares the stellar mass from the SED fits with that from the 3.6μm luminosity, and the right panel compares with the stellar mass from K_s luminosity. Both of these fluxes are themselves used in the SED fitting. Even with the large uncertainty estimates from the mock and Bayesian methods, the agreement between 3.6μm and K_S luminosities and the SED-derived stellar masses is very good.

in the SED fits. Still, these comparisons are an important consistency check of our fits, and also help provide a pathway toward comparing our SED-derived parameters with even broader samples from the literature.

Hα fluxes have been used to estimate SFRs for the LVL galaxies in Lee et al. (2009) as part of the 11HUGs project. We use their extinction-corrected Hα SFRs, which have been determined using the standard Kennicutt (1998) relationship with a dust correction as described in Lee et al. (2009), and follow a similar procedure for the BCD Hα fluxes. Figure 7 shows the comparison between our SED SFRs and the SFRs from Lee et al.

TABLE 6
Best fit values and Bayesian uncertainties for derived parameters of BCDs

Galaxy	$N_{\rm f}$	$\chi^2_{\rm r}$	log $M_{\star,o}$ [$M_\odot$]	log $M_{\star,y}$ [$M_\odot$]	$\langle SFR\rangle_{50}$ [$M_\odot$/yr]	τ_o [Gyr]	τ_y [Gyr]	age$_o$ [Gyr]	age$_y$ [Gyr]	$f_{\rm burst}$	A_V [mag]
(1)	(2)	(3)	(4)	(5)	(6)	(7)	(8)	(9)	(10)	(11)	(12)
UM323	9	0.3	8.13 (0.77)	6.10 (0.71)	0.124 (0.091)	5.1 (3.3)	0.42 (0.32)	3.6 (2.3)	0.76 (0.82)	0.16 (0.15)	0.32 (0.33)
UM408	8	0.1	8.06 (1.56)	5.91 (0.93)	0.081 (0.089)	4.9 (3.3)	0.39 (0.31)	3.4 (2.1)	0.88 (0.90)	0.18 (0.16)	0.19 (0.25)
Mk600	16	1.6	8.01 (0.37)	5.50 (0.35)	0.031 (0.010)	5.1 (3.3)	0.35 (0.29)	3.7 (2.4)	0.92 (0.85)	0.19 (0.15)	0.22 (0.03)
IIZw40	17	8.4	8.99 (0.64)	6.73 (0.20)	0.531 (0.101)	4.8 (3.3)	0.36 (0.30)	3.0 (1.7)	1.06 (1.01)	0.18 (0.15)	0.67 (0.03)
Mk5	15	8.9	8.21 (0.52)	5.23 (0.62)	0.018 (0.010)	4.1 (3.2)	0.29 (0.25)	4.0 (2.6)	0.89 (0.92)	0.15 (0.14)	0.30 (0.16)
CG10	8	0.4	7.73 (0.90)	5.45 (0.81)	0.027 (0.021)	4.7 (3.3)	0.44 (0.32)	3.6 (2.4)	0.87 (0.86)	0.14 (0.14)	0.20 (0.24)
IZw18	12	0.7	7.20 (0.64)	5.85 (0.30)	0.088 (0.027)	3.6 (3.0)	0.33 (0.28)	5.5 (3.0)	0.33 (0.02)	0.23 (0.15)	0.12 (0.06)
Was5	9	0.4	7.87 (0.95)	5.58 (1.04)	0.036 (0.034)	4.5 (3.3)	0.46 (0.33)	4.3 (2.8)	0.72 (0.78)	0.11 (0.12)	0.23 (0.28)
Mk36	14	2.5	7.02 (1.12)	5.45 (0.13)	0.023 (0.004)	4.0 (3.1)	0.53 (0.33)	4.2 (2.7)	0.33 (0.02)	0.18 (0.15)	0.10 (0.08)
UM439	9	0.3	7.96 (0.44)	5.93 (0.73)	0.099 (0.094)	5.3 (3.3)	0.38 (0.30)	3.7 (2.4)	0.69 (0.78)	0.20 (0.16)	0.15 (0.18)
Mk750	7	0.1	7.15 (1.00)	5.08 (0.93)	0.011 (0.011)	4.7 (3.3)	0.45 (0.32)	3.9 (2.6)	0.68 (0.76)	0.16 (0.15)	0.46 (0.39)
UM461	15	1.2	7.52 (0.56)	5.22 (0.32)	0.016 (0.005)	5.1 (3.3)	0.45 (0.33)	4.6 (2.9)	0.60 (0.59)	0.17 (0.15)	0.41 (0.26)
UM462	16	2.2	8.60 (0.65)	5.95 (0.20)	0.089 (0.018)	4.2 (3.2)	0.49 (0.33)	5.3 (3.0)	0.75 (0.79)	0.11 (0.12)	0.66 (0.03)
Mk67	10	0.7	7.88 (0.63)	5.70 (1.00)	0.057 (0.061)	4.8 (3.3)	0.37 (0.30)	4.1 (2.7)	0.72 (0.82)	0.17 (0.15)	0.34 (0.30)
Mk475	15	1.4	7.47 (0.78)	4.91 (0.44)	0.008 (0.003)	4.1 (3.2)	0.34 (0.29)	3.7 (2.4)	0.92 (0.87)	0.18 (0.16)	0.18 (0.13)
Mk900	15	3.6	9.18 (0.30)	5.79 (0.31)	0.060 (0.017)	2.5 (2.1)	0.42 (0.32)	5.3 (3.0)	2.09 (0.98)	0.28 (0.16)	0.21 (0.06)
Mk324	10	0.3	8.69 (0.71)	6.23 (1.30)	0.163 (0.192)	5.2 (3.3)	0.40 (0.31)	4.3 (2.7)	0.88 (0.85)	0.14 (0.14)	0.34 (0.35)
Mk328	10	0.4	8.87 (0.51)	6.14 (1.35)	0.130 (0.160)	3.9 (3.1)	0.38 (0.31)	4.2 (2.7)	1.17 (1.01)	0.12 (0.12)	0.43 (0.40)

Note. — Bayesian-like uncertainties are given in parentheses following values. Uncertainties on the logarithm of stellar mass (columns 4 & 5) are given as fractions of uncertainty divided by value (σ/value).

TABLE 7
Uncertainties and deviations of derived parameters

Param.	Bayesian avg. uncert.	Mock avg. dev.	empirical comp.
(1)	(2)	(3)	(4)
$\langle SFR\rangle_{10}$	0.62 ± 0.48	-0.04 ± 0.25	···
$\langle SFR\rangle_{50}$	0.58 ± 0.39	-0.03 ± 0.19	0.34[a]
$\langle SFR\rangle_{100}$	1.00 ± 0.42	0.06 ± 0.23	0.29[b]
$\langle SFR\rangle_{500}$	0.55 ± 0.26	0.03 ± 0.15	···
$\langle SFR\rangle_{1000}$	0.72 ± 0.29	-0.03 ± 0.19	···
$SFR_{\rm all}$	0.40 ± 0.14	-0.01 ± 0.07	···
$M_{\star,o}$	0.43 ± 0.18	0.02 ± 0.10	0.14[c]
$M_{\star,y}$	0.62 ± 0.48	-0.04 ± 0.25	···
age$_o$	0.54 ± 0.12	0.01 ± 0.10	···
τ_o	0.66 ± 0.20	-0.00 ± 0.13	···
age$_y$	0.90 ± 0.21	-0.01 ± 0.17	···
τ_y	0.76 ± 0.13	-0.02 ± 0.12	···
$f_{\rm burst}$	0.88 ± 0.23	-0.05 ± 0.15	···
$A_{\rm FUV}$	0.35 ± 0.38	0.01 ± 0.08	···
$A_{\rm V}$	0.40 ± 0.36	0.00 ± 0.10	···
α	0.15 ± 0.13	0.02 ± 0.05	···
δ	0.45 ± 0.21	-0.03 ± 0.12	···

Note. — Column 2: Average (and rms) of uncertainties from Bayesian-like analysis of PDFs (in dex). Column 3: Average (and rms) of deviations from mock analysis (in dex). Column 4: Scatter in comparison to observables (in dex): [a] from Hα observations, [b] from UV observations, [c] for total stellar mass from 3.6μm observations, Values are included in these averages for the 257 real fits and 162 mock fits with measured fluxes in all filters and $\chi^2_{\rm red} < 5$.

(2009) for the galaxies in common, and the same comparison using UV photometry. The Hα emission is most sensitive to star formation occurring over the past ∼10 Myrs while the shortest meaningful time scale we can measure SFR in the SED fits is ∼50 Myrs. Despite these timescale differences, the agreement is still quite good. The UV estimates of SFR are in better agreement with the 100 Myr-averaged SFH since the timescales are more closely matched, but the UV fluxes are themselves included in the SED-fitting.

The relationship between SED and Hα SFRs for the LVL galaxies shows generally good agreement, with a scatter of ∼0.3 dex. The Hα fluxes are not included in the SED fits, as it remains a challenge to incorporate them at low redshifts, but is often required for galaxies at higher redshifts (Ono et al. 2010; Stark et al. 2013; de Barros et al. 2014). In our case, the Hα fluxes give an independent estimate of the recent star formation in our sample, and allow us to assess the reliability of our SED fits. However, the SED fits rely primarily on UV fluxes to determine SFRs, while the Hα SFRs are measuring somewhat different star formation activity (see Section 5.1 for further discussion on the systematic offset between SFRs from Hα fluxes and SED fits for the BCDs).

Consistent with many previous studies, McGaugh & Schombert (2014) find that NIR luminosities of galaxies are a good tracer of their stellar mass, almost independently of their color (e.g., evolutionary state). They give mass-to-light ratios of M/L=0.6 $M_\odot/L_\odot$ in the K_s filter, and M/L=0.47$M_\odot/L_\odot$ in the 3.6μm band of Spitzer-IRAC (using Vega magnitudes). We use these mass-to-light ratios and our observed photometry to determine stellar masses for our galaxies, shown in Figure 8. For BCDs without Spitzer observations, we generate 3.6μm stellar masses from *w1* band photometry from the ALLWISE[8] catalog from the Wide-field Infrared Survey Explorer (Wright et al. 2010).

Figure 8 shows the generally good agreement between SED masses and luminosity-based estimates. This is unsurprising as the SED fits already use the same fluxes that are used to generate the masses via mass-to-light ratios. Still, these comparisons demonstrate that our SED-fitting methods produce stellar masses which are consistent with those found using simpler methods. Fur-

[8] http://wise2.ipac.caltech.edu/docs/release/allwise/

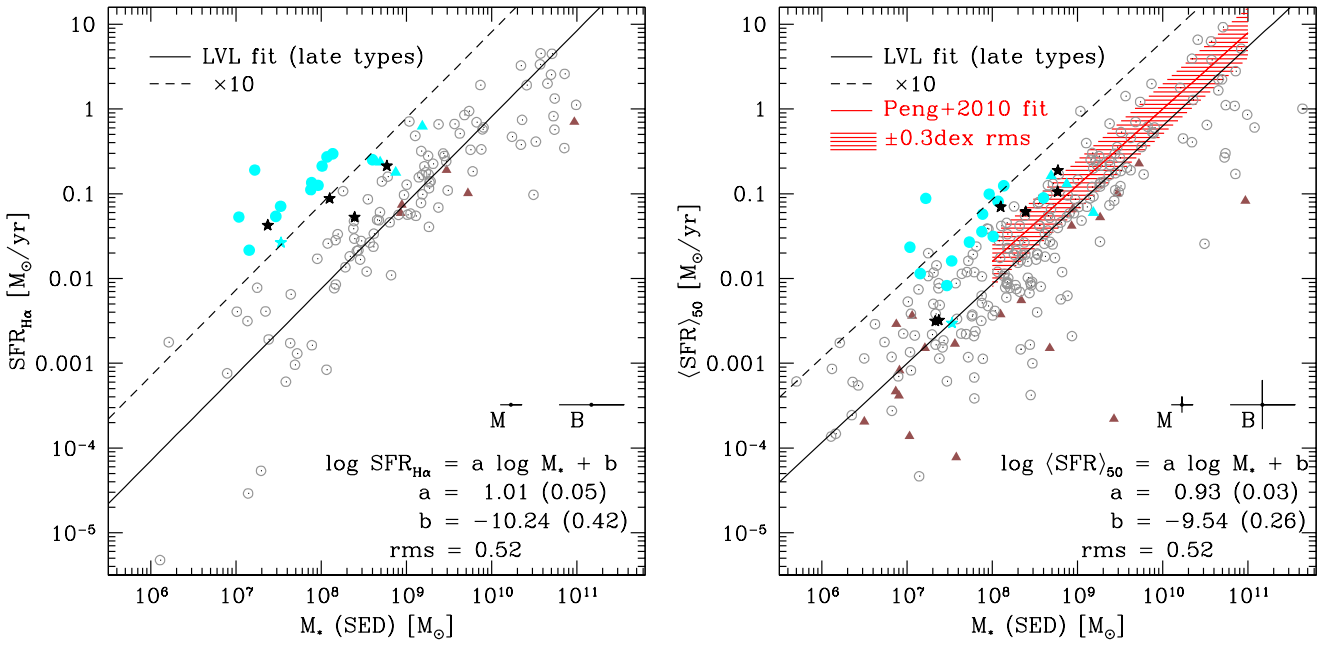

FIG. 9.— SFR versus stellar mass for the complete LVL and BCD samples (color-coding is the same as Figure 7. The left panel shows the SFR determined from Hα observations (for the galaxies with Hα measurements) while the right panel shows the 50-Myr average SFRs determined from the SED fits. Typical error bars are shown from mock ("M") and Bayesian ("B") analysis. The red shaded area corresponds to the relationship found by Peng et al. (2010) for $z\sim$0.1 SDSS galaxies. Both panels show the best-fit line from the late-type LVL galaxies, and its slope (a), intercept (b), and their uncertainties. The BCDs (from our sample and the LVL sample) have higher SFRs than typical galaxies of their mass, and are especially extreme in SFR$_{H\alpha}$.

ther, the small offset and lack of mass-trends in the relationships indicate that there are no significant mass-dependent systematic effects.

3.7. *Total uncertainty budget*

Putting all of these reliability and uncertainty estimates together, we now arrive at a complete error budget for our SED fit results, shown in Table 7. This includes the Bayesian-like uncertainties from the SED-fits, the mock analysis of reliability, and the external comparison with observations. In general, the uncertainties are small enough that it is possible to fit the SEDs of BCDs and LVL galaxies and reliably determine some of their physical parameters. In particular, we find that our estimates of stellar mass have a typical Bayesian uncertainty of $\sim$0.5 dex, but agree with empirical comparisons within 0.14 dex. Similarly our estimates of SFR on various time scales have formal Bayesian uncertainties between $0.40-1.00$ dex, but show significantly better agreement with empirical comparisons of $0.25-0.30$ dex, and mock deviations that are even smaller. These SED-derived parameters are not "high precision" measurements, but are constrained well enough to allow for meaningful comparisons between the BCD and LVL samples. These uncertainty estimates are included on all subsequent plots, and demonstrate the reliability and accuracy of the parameters.

4. RESULTS FROM SED FITS

Having generated best-fit parameters for the full sample of BCDs (shown in Table 6) and LVL galaxies, we can now compare these populations. To put the BCDs (from our sample and the LVL sample) into a broader context, we consider the non-BCD late-type galaxies in LVL as "normal" galaxies. We are interested in testing whether BCDs are best described as a phase of dI evolution, or whether BCDs represent a unique type of dwarf galaxy. While some of the SED-derived parameters are difficult to accurately and reliably determine, our fitting method is uniformly applied to the observations of the BCDs and LVL galaxies, so we can study the statistical trends between the two populations in a differential sense. In the following section we discuss the results of our SED fitting and the implications they have on the evolutionary context of BCDs.

4.1. *Stellar Mass vs SFR relation*

Figure 9 shows two versions of the M$_{stellar}$−SFR diagram, where the the late-type LVL galaxies populate the so-called "main sequence" of star-forming galaxies. We show measurements of the SFR from the SED fit averaged over 50 Myr and from Hα observations. As found by previous studies (e.g., the shaded area from Peng et al. 2010), there is a relatively tight relationship between SFR and stellar mass. The BCDs lie at (and above) the upper extreme of this relationship, in the sense that they have larger SFRs than most other galaxies of their stellar mass.

The relatively tight M−SFR relationship is typically interpreted as evidence of a universal mode of star formation in star-forming galaxies, where the global amount of star formation in a galaxy is regulated (in some way) by its stellar mass. This strong correlation between SFR and M$_{stellar}$ is seen across five orders of magnitude of mass. As discussed more extensively in Cook et al. (2014b), there is good agreement in the overlap between the relationship from the late-type LVL galaxies and that of Peng et al. (2010). The early-type LVL galaxies are typically offset below the best-fit line, as they have lower SF activity than comparable late-type galaxies. The LVL

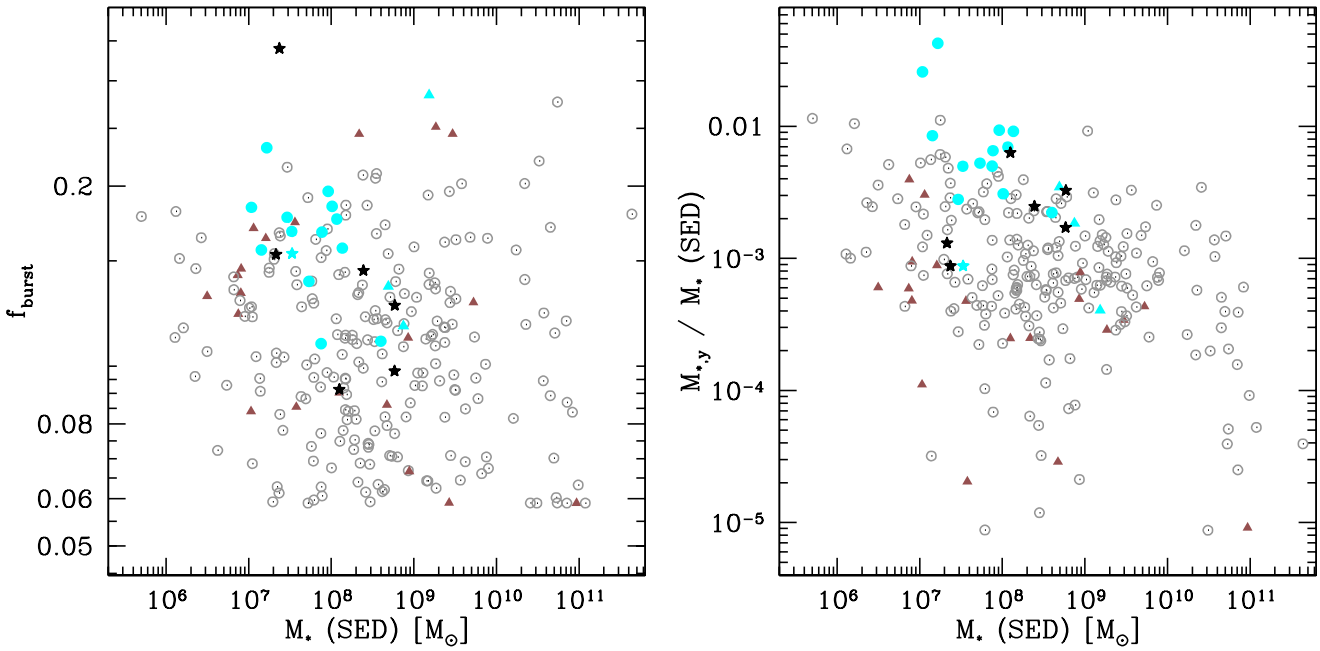

FIG. 10.— Left panel shows the relationship between $f_{\rm burst}$ (initial mass ratio of young population) and total stellar mass. Right panel shows the relationship between the present day young stellar population mass ratio as a function of total stellar mass. Color-coding is as in Figure 7. When compared with late-type LVL galaxies of similar total stellar mass, BCDs have more extreme young stellar population mass ratios (right panel) than burst fractions (left panel).

sample extends to significantly lower stellar masses than the SDSS sample, and confirms that the star-forming main sequence relationship continues at least down to $M_{\rm stellar}$ $\sim 10^6 M_\odot$, although it may become broader at the lower masses.

As seen in Figure 9, regardless of whether SFR is measured via the 50-Myr average from SED fits or from Hα fluxes, the M−SFR relationship for BCDs is offset from that of normal galaxies. When considering $\rm SFR_{H\alpha}$ measurements, the BCDs are more than an order of magnitude offset from the typical relationship, in the sense that BCDs have ∼10 times more star formation per unit stellar mass. When using $\langle \rm SFR \rangle_{50}$, the offset between the BCDs and normal galaxies is smaller, but is still nearly an order of magnitude. Regardless of the implicit assumptions in different SFR indicators, BCDs show SFRs elevated above the star-forming "main sequence", indicating that BCDs are experiencing truly exceptional amounts of star formation. As their Hα SFRs are elevated beyond the SED SFRs (based on UV fluxes), the current SF in BCDs may also be especially recent.

4.2. *Burst strength*

As part of its SED-fitting process, CIGALE determines the "burst fraction" ($f_{\rm burst}$) for each galaxy, defined as the initial mass fraction of the young stellar population. More explicitly, this is the mass fraction of the young stellar population compared to the total stellar mass, *which are both taken at the time of the young population's birth.* The present-day mass ratio of the young stellar population will always be smaller than the initial $f_{\rm burst}$ as the young high mass stars are perishing at a faster rate than the older stellar populations.

Figure 10 shows both the initial $f_{\rm burst}$ and the present-day young stellar population mass ratio as functions of total stellar mass. There is a substantial overlap between the late-type LVL galaxies and BCDs in terms of their initial $f_{\rm burst}$ values (left panel), which may mean that BCDs and non-BCDs may have experienced similarly strong starbursts in their past. However, BCDs with lower stellar masses typically have higher initial $f_{\rm burst}$ values, which is consistent with a single star formation event having a more significant effect on a lower mass galaxy. One of the BCD/E galaxies, Mk 900, has $f_{\rm burst} = 0.28$ and is an exception to this trend. Its young stellar population is the oldest among the BCD sample fits (age$_y$=2 Gyr), so its burst strength is also the most extreme. Note that its young population mass ratio ($M_{\star,y}/M_\star$) is $\sim 10^{-3}$, which is typical for other galaxies of its mass.

While there is overlap between BCDs and late-type LVL galaxies, the BCD population is offset higher than normal galaxies, suggesting that the star forming events (in terms of the mass involved) may be more substantial in BCDs.

When considering the young stellar population mass ratio (shown in the right panel of Figure 10), the BCDs more clearly populate the extreme of the parameter space. While BCDs and non-BCDs galaxies may have had more similar values of initial burst strengths (left panel), the mass fraction of today's young stellar population is much greater in BCDs than in LVL galaxies (right panel). Much of this difference is due to the age of their young stellar populations. BCDs have a significant young star-forming population, while the stellar populations in non-BCDs have had more time to age and fade. Again there is a trend for BCDs with lower stellar masses to have larger young population mass fractions.

Combined, the two panels of Figure 10 suggest that the young stellar populations of BCDs are different from normal late-type galaxies today. Their SED-derived burst strength does not separate them as clearly, but their

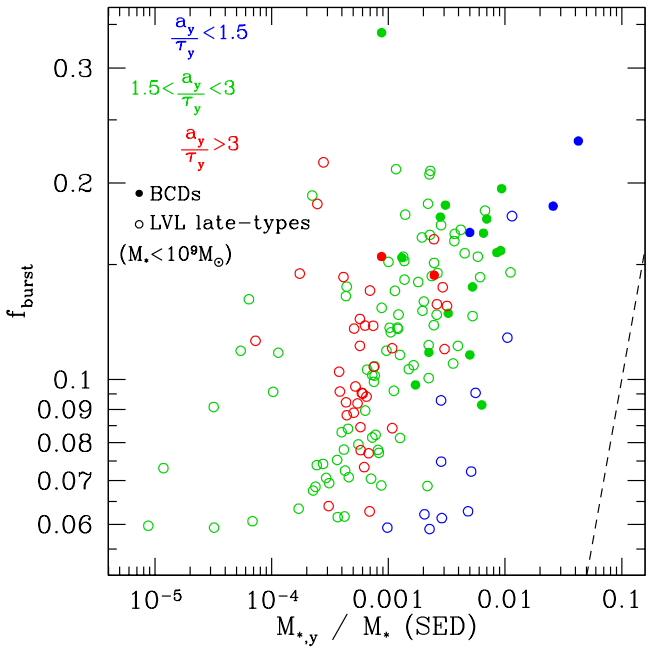

FIG. 11.— Comparison between best-fit $f_{\rm burst}$ values and estimates of the current mass ratio of the young stellar population. Each galaxy is plotted with a shape and color that correspond to the age of its young burst population, in units of its scale time, τ. Galaxies with bursts of age/τ<1.5 are shown in blue, middle-aged bursts are shown in green, and older bursts are shown in red. Solid dots show BCDs (from our sample and LVL) and open circles show late-type LVL galaxies, selected to be in the same stellar mass range as the BCDs. The dashed diagonal line shows the unity line, which indicates a very recent burst. The galaxy with the highest $f_{\rm burst}$ value is UGCA 281, an LVL galaxy classified as a BCD and discussed further in Section 4.2. The galaxy with the highest $M_{*,y}/M_*$ is I Zw 18. In general, BCDs are characterized by having both strong burst strength and a significant young population at present day, although there is substantial scatter.

young population is usually more significant. Furthermore, the exponential scale times associated with the young and old stellar populations can vary, which can add to the differences between these comparisons.

Further insight can be gained by combining these two estimates of burst strength into Figure 11, which shows $f_{\rm burst}$ as a function of the young stellar population mass ratio. The points on Figure 11 are color-coded by their young population burst age (age$_y$) divided by its exponential scale time (τ_y). Blue points show galaxies with young populations younger than 1.5τ, which are very recent bursts. Green points show middle-aged bursts, and red points show more evolved bursts. We plot all of the BCDs as dots (from our sample and the LVL sample) and the LVL late-type galaxies as circles. We only show galaxies from LVL in the stellar mass range ($M_* < 10^9 M_\odot$), to match the BCD sample.

If the young population bursts were extremely recent, the points would lie very close to the equality line (shown as a dashed diagonal line, where $f_{\rm burst}=M_{*,y}/M_*$). As the young population evolves, the points move horizontally in this plot as the young stellar population mass ratio decreases (while its initial burst fraction always remains the same). This is seen on the plot as the points closest to the 1:1 line have younger bursts (i.e. are blue points), although there is significant scatter beyond this simple trend due to different age$_y/\tau_y$ parameters of the SFHs. Compared with the late-type LVL galaxies, on average the BCDs show higher values of both $f_{\rm burst}$ and young population mass ratios, as expected.

With this relationship in mind, it appears that the star formation in BCDs is both substantial and typically more recent (than LVL). Note that some of the late-type galaxies in LVL have similar young populations to BCDs. The requirements of recent and substantial young stellar population are necessary, but not sufficient, criteria for a galaxy to be a BCD.

It is interesting to note that Figure 11 also shows a population of LVL galaxies with moderate initial $f_{\rm burst}$ (e.g., > 0.1) but with low present-day young population mass fraction (e.g., $< 0.5\%$). These characteristics are similar to what we would expect from a population of post-burst BCDs. When the young populations in those galaxies with high $f_{\rm burst}$ first started forming stars, by definition their young population mass fraction would have been equivalent to $f_{\rm burst}$. While we do not have any objects in our sample with young population mass fractions as extreme as 10%, galaxies in this state would unambiguously be considered starbursting systems (and possibly BCDs).

The young population burst ages of the BCDs (shown in Table 6) are somewhat larger than might be expected. Some of the most extreme BCDs have young population ages $<$ 500 Myr (e.g., I Zw 18 and Mk 36), but many have young population ages between 500 and 1000 Myr, and some even $>$ 1000 Myr. However, based on the strong Hα emission from the BCDs, it is unlikely that their young populations can be this old. Instead, this over-estimate of burst age demonstrates a limitation of our SED fits. The broadband fluxes used in the SED fit are most sensitive to star formation on 100-1000 Myr timescales, but only crudely and with low resolution. Even if the BCDs have had recent (50-100 Myr) star formation events, the SED fits are unable to resolve SFH changes on such short timescales. In this way, the SED fits are almost certainly systematically under-estimating the current star formation rates of galaxies which have recently started forming stars, which is consistent with the behavior seen in Figure 9.

As an alternative parametrization of the significance of the current star formation episode, we also calculate the birthrate parameter of Kennicutt (1983), defined as:

$$b = \frac{\rm SFR}{\langle \rm SFR \rangle} \qquad (2)$$

where b is the birthrate parameter, SFR is an estimate of the current SFR, and $\langle$SFR$\rangle$ is the total lifetime average SFR. This parameter is related to the specific star formation rate and also to the young stellar population mass fraction and $f_{\rm burst}$, but now parametrizes the starburst in terms of its star formation rate instead of the mass of the young stellar population .

We make two versions of b, one calculated using the most recent 50-Myr averaged SFR (b_{50}) as the numerator and one with the SFR determined from Hα observations ($b_{\rm H\alpha}$) as the numerator. In both cases, the denominator is the lifetime average SFR from the SED fits (closely related to the total stellar mass). These birthrate parameters are plotted as a function of stellar mass in Figure 12. As discussed previously, the Hα SFR is more sensitive to

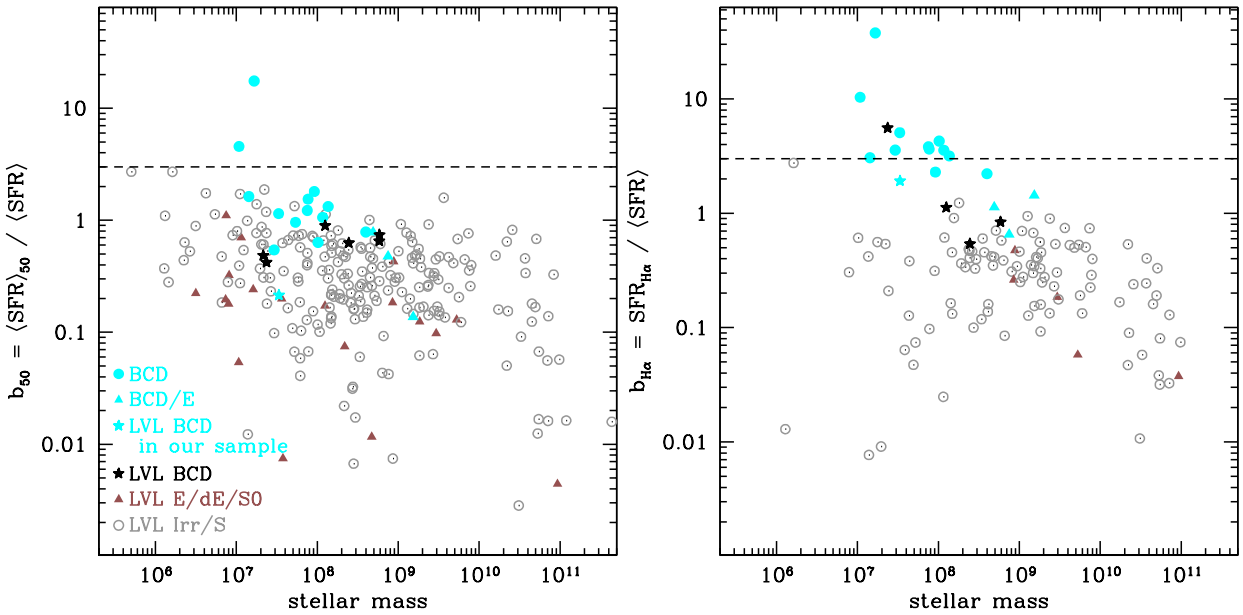

FIG. 12.— Left panel shows the 50-Myr averaged birthrate (b_{50}), and right panel shows the birthrate based on $SFR_{H\alpha}$ ($b_{H\alpha}$), with color scheme as earlier. Very few galaxies meet the $b \geq 3$ threshold for starbursts when using SFR_{50} from the SED fits, but the Hα-determined SFR shows many of the BCDs above the starburst threshold. The BCDs have higher birthrate parameters than the late-type LVL galaxies, but some LVL galaxies also have large values of b.

recent intense star formation, while the SED SFR probes longer time scales.

Note that these birthrate parameters are not measuring the stellar mass involved in the star formation event, but represent the significance of the current star formation in comparison with a galaxy's total lifetime of star formation. For a particular galaxy, the birthrate parameter describes the significance of its current star formation in its long-term evolution. A galaxy with a birthrate parameter of $b \geq 3$ is typically required to be considered a starburst (e.g., Bergvall et al. 2015, and references therein). In the smallest dwarf galaxies, the effects of star formation can be more significant (i.e., the effects of feedback on galaxy-wide scales) than the same absolute amount of star formation in larger galaxies. The birthrate parameter gives a good indication of the significance of the current SFR. Starbursting galaxies with $b > 3$ typically are undergoing a truly transformative event, distinct from the low-level fluctuations in SFR which are typical in dwarf galaxies.

In Figure 12, the b values for the BCDs show the correlation with stellar mass in the sense that lower stellar masses have larger b values, in the same way as $f_{\rm burst}$ and the young population mass fraction increased at lower stellar masses. This behavior is expected if the starbursts are similar in size, but can have a greater impact on a lower mass galaxy than on a higher mass galaxy. When comparing the b values for the BCD and LVL samples, the BCDs have values which are at or beyond the maximum values from the LVL non-BCD samples. In particular, one LVL galaxy also populates this extreme area: UGCA 281, which has long been classified as a BCD (Thuan & Martin 1981; Lelli et al. 2014). On the other hand, some members of our BCD sample (notably the three most massive galaxies: Mk 324, Mk 328, and Mk 900) populate the more normal areas of parameter space. The early-type galaxies from the LVL sample (red triangles) and the BCD/Es (cyan triangles) have some of the lowest values. These are also at somewhat higher masses, so a star formation event may have a smaller impact on their evolution.

Whether measured by the 50-Myr average from SED fits or by Hα fluxes, the birthrate parameters for BCDs are extreme, and show that the current star formation in BCDs is proceeding at a level which is not typical for normal star-forming galaxies.

5. DISCUSSION

While our SED fits can only generate coarse estimates of key physical parameters (e.g., $M_\star$, SFR) for the complete LVL sample and our BCDs, they still provide a systematic and meaningful way to compare the BCDs with normal LVL galaxies. Our SED fits have shown that BCDs are forming stars at exceptionally intense rates and may populate an elevated relation parallel to the "star formation main sequence." However, the SED fits cannot provide the detailed star formation histories which would be needed to clearly identify both past and present intense (but unsustained) levels of star formation in order to separate BCDs (both past and present) from normal dIs. Much of the detailed information about a galaxy's SFH is not accessible through SED fits alone, but can only be probed via studies of resolved stellar populations (e.g., McQuinn et al. 2015c). However, our SED fits can still be used to discuss and constrain the possible evolutionary connections between dwarf galaxies.

5.1. *SFR and stellar mass indicators at the extremes*

Most of the empirical SFR and stellar mass indicators (e.g., Kennicutt 1998; McGaugh & Schombert 2014) have been calibrated using galaxies with large stellar masses ($M_\star \approx M_{\rm MWG}$), with modest abundances ($Z \approx Z_\odot$), and star formation rates (SFR$\approx 1 M_\odot$/yr). More recently, some groups have been able to test whether these stan-

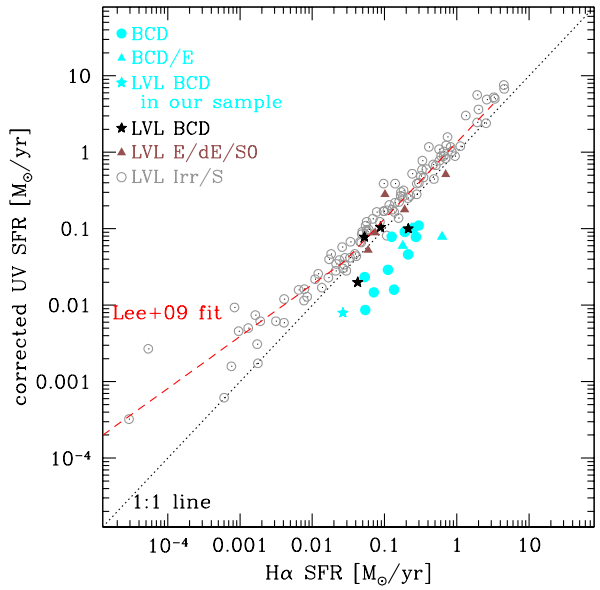

FIG. 13.— This figure shows the correlation between observed SFRs from Hα fluxes and UV fluxes (corrected for internal extinction). LVL galaxies are shown in black, and BCDs in blue. In black is the equality line. The offset between BCDs and LVL galaxies is likely due to assumptions in the empirical conversion factors about SFH, which the BCDs do not obey. The red line shows the best fit relation from Lee et al. (2009).

dard relations apply equally well to galaxies with lower masses, lower abundances, and possibly higher SFRs.

Lee et al. (2009) found that for galaxies with low SFR, Hα measurements give systematically lower SFRs than are measured in the UV. Similar findings have been reported by other groups as well (Fumagalli et al. 2011; Eldridge 2012; Weisz et al. 2012). We can also compare the SFRs for the galaxies in our sample, as shown in Figure 13, and plot SFR from Hα against SFR from UV. The best fit relation from Lee et al. (2009) is also shown, and matches the same general trend as the LVL data.

The BCDs appear offset from the main population in Figure 13, which is similar to the offsets previously seen in the SFR comparisons (e.g., Figure 7). As mentioned in Section 3.6, the BCDs have systematically larger $\mathrm{SFR}_{\mathrm{H}\alpha}$ than $\langle\mathrm{SFR}\rangle_{50}$, while their $\mathrm{SFR}_{\mathrm{UV}}$ and $\langle\mathrm{SFR}\rangle_{100}$ estimates are in better agreement. A similar offset in the BCD $\mathrm{SFR}_{\mathrm{H}\alpha}$ estimates is seen here in Figure 13.

A possible explanation for this offset lies in the calibration of these SFR indicators. The empirical SFR estimates used to generate $\mathrm{SFR}_{\mathrm{UV}}$ and $\mathrm{SFR}_{\mathrm{H}\alpha}$ both assume a constant SFR. In the FUV, the flux comes from young stars with lifetimes $\sim10^8$ years, and correspondingly measures the SFR on those time scales. The Hα flux comes from gas ionized by massive O-stars and early-type B-stars, with shorter lifetimes than those providing UV flux. As such, the Hα-derived SFR probes shorter time scales.

Lee et al. (2009) argue that the change of this relationship at low SFRs may be due to stochastic variations in the SFH of low mass galaxies, where the UV SFR averages over longer time scales and will typically be larger than the Hα SFR in the case of a bursty SFH. As shown in Figure 13, the BCDs (from our sample and from within LVL) nearly always have larger Hα SFRs than UV SFRs. This suggests that the BCDs may be in a phase of their SFH where intense star formation has only recently begun, and is better traced by the Hα SFR than by UV. The best-fit SFRs from the SED fits are driven by the UV emission, and as such are not sensitive to the recent star formation which produces Hα emission. If the BCDs have had a recent enhancement in SF activity, the UV SFR measurement could be diluted by the lower SF which may have preceded the current event.

5.2. *Outliers and exceptional galaxies*

The comparisons from Section 3.6 between empirical estimates of stellar mass (via 3.6μm and K_s luminosity) and SFR (via Hα and UV luminosity) with those from the SED fits were primarily intended as consistency checks of the SED fitting process. However, they can also be used to test the reliability of different stellar mass and SFR estimators for particular objects. For most galaxies in our sample, the SED fitting gives SFR and stellar mass values consistent with the empirical methods. However, the galaxies with inconsistent values require further investigation. There can be many reasons for individual galaxies to deviate from the normal relationships: they may be intrinsically unusual objects in a brief evolutionary stage or an uncommon region of parameter space, or may be examples of objects which have SEDs that are not well fit by our methods. Here we look at individual objects from the previous figures as examples of the types of outliers in this work.

As shown in Section 3.6, the SED-derived stellar masses are generally in good agreement with the empirical estimates from 3.6μm and K_s luminosity measurements. We have identified only very slight offsets or non-unity slopes in these relationships. On the 3.6μm plot in the left panel of Figure 8, there are no significant outliers from the distribution of points. On the right panel of Figure 8 which shows the stellar mass from K_s photometry, the object furthest above the relation is a BCD (UM 462) and the object furthest below the relation is an LVL galaxy (UGC 01056). UM 462 has a SED-derived stellar mass $\sim$50% larger than its K_s mass, and UGC 01056 has an SED-mass $\sim$50% smaller than its K_s mass. These deviations are still within the Bayesian estimates of uncertainty on the SED fits, and represent the most deviant mass estimates.

Throughout this analysis it has become clear that some members of our BCD sample are less extreme than others. In particular, Mk 324, Mk 328, and Mk 900 (labeled as "BCD/E" on the figures) typically have properties more similar to the average LVL late-type galaxies. Similarly, Janowiecki & Salzer (2014) found that these three were the reddest (B$-$V$\sim$0.8 in their outskirts), most luminous, and most metal-rich objects in this BCD sample. The SED fits have shown that these three also have the largest stellar masses ($\mathrm{M}_\star > 4\times10^8 M_\odot$) and the lowest specific star formation rates ($\mathrm{SSFR} < 3\times10^{-10}$ /yr) of the BCD sample. Given the dissimilarities between the three objects and the rest of the BCD sample, we advise caution when drawing conclusions about BCDs based on the inclusion of these three objects. They have been included in our sample to cover the broad range of objects commonly referred to as BCDs, but may be more intermediate between extreme BCDs and more typical dwarf irregular galaxies.

5.3. *Future evolution of BCDs*

With their short gas depletion time scales and rapid star formation rates, BCDs are in an unsustainable evolutionary state, and cannot continue forming stars at their current rate. Many groups have studied or discussed the implications of a population of faded or post-burst BCDs (Sánchez Almeida et al. 2008, 2009; Amorín et al. 2012; Lelli et al. 2012; Koleva et al. 2013; Janowiecki & Salzer 2014; Meyer et al. 2014). Here it is important to separate possible evolutionary pathways based on whether external or internal effects are being considered.

Meyer et al. (2014) consider the long-term evolution of BCDs in the Virgo Cluster, and find that BCDs may fade into galaxies similar to the extant population of early type dwarfs in the Virgo Cluster. They further suggest that in the cluster environment, a compact early type dwarf may have its star formation reignited if it acquires fresh gas. In lower density environments, Sánchez Almeida et al. (2008) searched for BCDs in quiescence (QBCDs) by selecting galaxies with compact structural parameters and other BCD-like properties, but without the current intense star formation event. Within their search criteria, they found a very large population of QBCDs, and suggest that perhaps 1/3 of all local dwarf galaxies may be capable of hosting a BCD-like burst. Whether such intense starbursts are this common is still an open question.

In this work, some of the SED-derived parameters for the BCDs and LVL galaxies will evolve with time, while others will not. For example, the initial burst fraction ($b_{\rm frac}$) of the current star star forming population will not decrease with time, while the young population mass fraction will continue to decline. Similarly, the total stellar mass will not change quickly, while the color will shift from blue to red as the hottest youngest stars perish. We can generate model predictions for the future evolution of BCDs, but this requires that we assume there are no external effects driving this evolution.

In the simple case of internal evolution only, the stellar populations of the BCDs would age normally, and follow the characteristic isochrones for older ages. The resulting objects may resemble the so-called "postburst" galaxies (or E+A, k+a, a+k, Dressler & Gunn 1983; Dressler et al. 1999). These galaxies are characterized by strong Balmer line absorption (from the most massive stars still alive, the A stars), but no Hα emission (as the O and B stars have perished). Other groups have used the 4000Å break (Kauffmann et al. 2003) or star formation histories from resolved stellar populations (McQuinn et al. 2010a,b) to identify galaxies which have experienced strong star formation events. Further followup on individual post-BCD-like galaxies is necessary to explore this connection further.

6. SUMMARY

In this work we have used panchromatic observations (from UV to FIR) of a large sample of 258 LVL galaxies and 18 BCDs to generate and fit SEDs in order to determine key physical parameters about these galaxies. These fits have allowed us to explore the role that BCDs play in the larger context of dwarf galaxy evolution. In particular, our main results are as follows:

– Our SED fits are able to reliably and robustly estimate key physical parameters of these galaxies, including $M_\star$ and various SFRs.

– SED model grids must be chosen to be broad and well-sampled enough to cover appropriate parameter space or else the best-fit values may have systematic offsets or errors.

– Two-burst stellar population models fit the observed SEDs significantly better than one-burst models, suggesting that most or all dwarf galaxies have an old stellar population.

– While powerful, the inability of SED fits to return a detailed SFH makes it difficult to answer questions about the evolutionary histories of individual BCDs.

– When using Hα SFRs in place of SED SFRs, the BCDs appear even more extreme than typical galaxies, suggesting that the SF activity in BCDs is uniquely intense or recent, and that SED fits are not sensitive to the recent star formation traced by Hα emission.

– We have identified unusual and potentially extreme objects for further study, which may represent brief evolutionary stages in dwarf galaxy evolution.

Further work is needed to more completely explore the evolutionary relationships between LVL galaxies and BCDs, and to connect the SED-fit results with the compactness estimates of Janowiecki & Salzer (2014). Once available, the optical surface photometry of the LVL galaxies will provide an invaluable resource for a more complete comparison between the BCDs and LVL galaxies. We will be able to determine how extreme the BCDs are both in terms of the structural parameters of their underlying hosts and in terms of their stellar populations. BCDs appear to represent an extreme class of dwarf galaxy with physical properties that place them at the edges of the broad continuum of dwarf galaxy properties.

7. ACKNOWLEDGMENTS

SJ is grateful to D. Cook for providing the LVL SEDs and metallicities in a convenient format, and to S. Salim and H. Evans for useful discussions and advice. We thank the anonymous referee for helping to improve, clarify, and expand the context of this work. All SED analysis was run on a laptop purchased with funds from a McCormick Science Grant from the Indiana University College of Arts and Sciences. Some results from this work were also presented in Janowiecki (2015). Support is acknowledged from GALEX Cycle 3 program GI3-089. SJ acknowledges support from the Australian Research Council's Discovery Project funding scheme (DP150101734).

This research has made use of NASA's Astrophysics Data System Bibliographic Services. This research has also made use of the NASA/IPAC Extragalactic Database (NED), which is operated by the Jet Propulsion Laboratory, California Institute of Technology, under contract with the National Aeronautics and Space Administration.

Funding for SDSS-III has been provided by the Alfred P. Sloan Foundation, the Participating Institutions, the National Science Foundation, and the U.S. Department of Energy Office of Science. The SDSS-III web site is http://www.sdss3.org.

SDSS-III is managed by the Astrophysical Research Consortium for the Participating Institutions of the SDSS-III Collaboration including the University of Arizona, the Brazilian Participation Group, Brookhaven National Laboratory, University of Cambridge, Carnegie Mellon University, University of Florida, the French Participation Group, the German Participation Group, Harvard University, the Instituto de Astrofisica de Canarias, the Michigan State/Notre Dame/JINA Participation Group, Johns Hopkins University, Lawrence Berkeley National Laboratory, Max Planck Institute for Astrophysics, Max Planck Institute for Extraterrestrial Physics, New Mexico State University, New York University, Ohio State University, Pennsylvania State University, University of Portsmouth, Princeton University, the Spanish Participation Group, University of Tokyo, University of Utah, Vanderbilt University, University of Virginia, University of Washington, and Yale University.

REFERENCES

Alam, S., Albareti, F. D., Allende Prieto, C., et al. 2015, ApJS, 219, 12
Aloisi, A., Clementini, G., Tosi, M., et al. 2007, ApJ, 667, L151
Amorín, R., Pérez-Montero, E., Vílchez, J. M., & Papaderos, P. 2012, ApJ, 749, 185
Ashley, T., Elmegreen, B. G., Johnson, M., et al. 2014, AJ, 148, 130
Baldwin, J. A., Spinrad, H., & Terlevich, R. 1982, MNRAS, 198, 535
Bauer, A. E., Hopkins, A. M., Gunawardhana, M., et al. 2013, MNRAS, 434, 209
Bekki, K. 2008, MNRAS, 388, L10
Bell, E. F., & de Jong, R. S. 2001, ApJ, 550, 212
Berg, D. A., Skillman, E. D., Marble, A. R., et al. 2012, ApJ, 754, 98
Bergvall, N., Marquart, T., Way, M. J., et al. 2015, A&A, accepted, arXiv:1501.06928
Bordalo, V., Plana, H., & Telles, E. 2009, ApJ, 696, 1668
Brinchmann, J., Charlot, S., White, S. D. M., et al. 2004, MNRAS, 351, 1151
Brinchmann, J., Pettini, M., & Charlot, S. 2008, MNRAS, 385, 769
Bruzual, G., & Charlot, S. 2003, MNRAS, 344, 1000
Buat, V., Giovannoli, E., Takeuchi, T. T., et al. 2011, A&A, 529, AA22
Calzetti, D., Armus, L., Bohlin, R. C., et al. 2000, ApJ, 533, 682
Cardelli, J. A., Clayton, G. C., & Mathis, J. S. 1989, ApJ, 345, 245
Carigi, L., Colin, P., Peimbert, M., & Sarmiento, A. 1995, ApJ, 445, 98
Cook, D. O., Dale, D. A., Johnson, B. D., et al. 2014, MNRAS, 445, 899
Cook, D. O., Dale, D. A., Johnson, B. D., et al. 2014, MNRAS, 445, 881
Croxall, K. V., van Zee, L., Lee, H., et al. 2009, ApJ, 705, 723
Daddi, E., Dickinson, M., Morrison, G., et al. 2007, ApJ, 670, 156
Dale, D. A., Cohen, S. A., Johnson, L. C., et al. 2009, ApJ, 703, 517
Dale, D. A., Helou, G., Magdis, G. E., et al. 2014, ApJ, 784, 83
de Barros, S., Schaerer, D., & Stark, D. P. 2014, A&A, 563, A81
Deason, A., Wetzel, A., & Garrison-Kimmel, S. 2014, ApJ, 794, 115
Dressler, A., & Gunn, J. E. 1983, ApJ, 270, 7
Dressler, A., Smail, I., Poggianti, B. M., et al. 1999, ApJS, 122, 51
Eldridge, J. J. 2012, MNRAS, 422, 794
Elmegreen, B. G., Zhang, H.-X., & Hunter, D. A. 2012, ApJ, 747, 105
Fumagalli, M., da Silva, R. L., & Krumholz, M. R. 2011, ApJ, 741, L26
Gil de Paz, A., Madore, B. F., & Pevunova, O. 2003, ApJS, 147, 29
Giovannoli, E., Buat, V., Noll, S., Burgarella, D., & Magnelli, B. 2010, SF2A-2010: Proceedings of the Annual meeting of the French Society of Astronomy and Astrophysics, 41
Guseva, N. G., Izotov, Y. I., Papaderos, P., et al. 2001, A&A, 378, 756
Hunter, D. A., & Hoffman, L. 1999, AJ, 117, 2789
Inoue, A. K. 2011, MNRAS, 415, 2920
Inoue, A. K., Buat, V., Burgarella, D., et al. 2006, MNRAS, 370, 380
Izotov, Y. I., & Thuan, T. X. 2004, ApJ, 616, 768
Izotov, Y. I., & Thuan, T. X. 1999, ApJ, 511, 639
Izotov, Y. I., Thuan, T. X., & Lipovetsky, V. A. 1994, ApJ, 435, 647
Izotov, Y. I., Thuan, T. X., & Stasińska, G. 2007, ApJ, 662, 15
Janowiecki, S., & Salzer, J. J. 2014, ApJ, 793, 109
Janowiecki, S. 2015, Ph.D Thesis (Indiana University) ProQuest, 290, 3718472
Johnson, R. A., Lawrence, A., Terlevich, R., & Carter, D. 1997, MNRAS, 287, 333
Kauffmann, G., Heckman, T. M., White, S. D. M., et al. 2003, MNRAS, 341, 33
Kennicutt, R. C., Jr. 1983, ApJ, 272, 54
Kennicutt, R. C., Jr. 1998, ARA&A, 36, 189
Kennicutt, R. C., Jr., Lee, J. C., Funes, S. J., José G., Sakai, S., & Akiyama, S. 2008, ApJS, 178, 247
Kewley, L. J., & Ellison, S. L. 2008, ApJ, 681, 1183
Kobulnicky, H. A., & Kewley, L. J. 2004, ApJ, 617, 240
Koleva, M., Bouchard, A., Prugniel, P., De Rijcke, S., & Vauglin, I. 2013, MNRAS, 428, 2949
Lee, J. C., Gil de Paz, A., Tremonti, C., et al. 2009, ApJ, 706, 599
Lee, J. C., Gil de Paz, A., Kennicutt, R. C., Jr., et al. 2011, ApJS, 192, 6
Leitherer, C., Li, I.-H., Calzetti, D., & Heckman, T. M. 2002, ApJS, 140, 303
Lelli, F., Verheijen, M., Fraternali, F., & Sancisi, R. 2012, A&A, 544, AA145
Lelli, F., Verheijen, M., & Fraternali, F. 2014, A&A, 566, AA71
Loose, H.-H., & Thuan, T. X. 1986, ApJ, 309, 59
Mac Low, M.-M., & Ferrara, A. 1999, ApJ, 513, 142
Marble, A. R., Engelbracht, C. W., van Zee, L., et al. 2010, ApJ, 715, 506
Martin, D. C., Fanson, J., Schiminovich, D., et al. 2005, ApJ, 619, L1
Matteucci, F., & Chiosi, C. 1983, A&A, 123, 121
McGaugh, S. S. 1991, ApJ, 380, 140
McGaugh, S. S., & Schombert, J. M. 2014, AJ, 148, 77
McQuinn, K. B. W., Skillman, E. D., Cannon, J. M., et al. 2009, ApJ, 695, 561
McQuinn, K. B. W., Skillman, E. D., Cannon, J. M., et al. 2010, ApJ, 724, 49
McQuinn, K. B. W., Skillman, E. D., Cannon, J. M., et al. 2010, ApJ, 721, 297
McQuinn, K. B. W., Cannon, J. M., Dolphin, A. E., et al. 2015a, ApJ, 802, 66
McQuinn, K. B. W., Skillman, E. D., Dolphin, A., et al. 2015b, ApJ, 815, L17
McQuinn, K. B. W., Lelli, F., Skillman, E. D., et al. 2015, MNRAS, 450, 3886
Meiksin, A. 2006, MNRAS, 365, 807
Meixner, M., Smee, S., Doering, R. L., et al. 2010, PASP, 122, 451
Meyer, H. T., Lisker, T., Janz, J., & Papaderos, P. 2014, A&A, 562, AA49
Morrissey, P., Conrow, T., Barlow, T. A., et al. 2007, ApJS, 173, 682
Moustakas, J., & Kennicutt, R. C., Jr. 2006, ApJS, 164, 81
Moustakas, J., Kennicutt, R. C., Jr., Tremonti, C. A., et al. 2010, ApJS, 190, 233
Noeske, K. G., Faber, S. M., Weiner, B. J., et al. 2007, ApJ, 660, L47
Noeske, K. G., Papaderos, P., Cairós, L. M., & Fricke, K. J. 2005, A&A, 429, 115
Noeske, K. G., Papaderos, P., Cairós, L. M., & Fricke, K. J. 2003, A&A, 410, 481
Noll, S., Burgarella, D., Giovannoli, E., et al. 2009, A&A, 507, 1793
Norton, S. 1997, "Structural Parameters of Blue Compact Dwarf Galaxies" (Honors Thesis). Wesleyan University
Ono, Y., Ouchi, M., Shimasaku, K., et al. 2010, ApJ, 724, 1524
Papaderos, P., Guseva, N. G., Izotov, Y. I., & Fricke, K. J. 2008, A&A, 491, 113
Papaderos, P., Loose, H.-H., Fricke, K. J., & Thuan, T. X. 1996, A&A, 314, 59
Peng, Y.-j., Lilly, S. J., Kovač, K., et al. 2010, ApJ, 721, 193
Pilyugin, L. S., & Thuan, T. X. 2005, ApJ, 631, 231

Sánchez Almeida, J., Muñoz-Tuñón, C., Amorín, R., et al. 2008, ApJ, 685, 194
Sánchez Almeida, J., Aguerri, J. A. L., Muñoz-Tuñón, C., & Vazdekis, A. 2009, ApJ, 698, 1497
Salim, S., Charlot, S., Rich, R. M., et al. 2005, ApJ, 619, L39
Salim, S., Rich, R. M., Charlot, S., et al. 2007, ApJS, 173, 267
Salim, S., Dickinson, M., Michael Rich, R., et al. 2009, ApJ, 700, 161
Salim, S., Lee, J. C., Janowiecki, S., et al. 2016, ApJS, 227, 2
Salzer, J. J., & Elston, R. 1992, The Stellar Populations of Galaxies, 149, 482
Sargent, W. L. W., & Searle, L. 1970, ApJ, 162, L155
Schlegel, D. J., Finkbeiner, D. P., & Davis, M. 1998, ApJ, 500, 525
Searle, L., & Sargent, W. L. W. 1972, ApJ, 173, 25
Stark, D. P., Schenker, M. A., Ellis, R., et al. 2013, ApJ, 763, 129
Sudarsky, D. L. 1995, "Stellar Populations of Blue Compact Dwarf Galaxies" (Honors Thesis). Wesleyan University
Terlevich, R., Melnick, J., Masegosa, J., Moles, M., & Copetti, M. V. F. 1991, A&AS, 91, 285
Thuan, T. X., & Martin, G. E. 1981, ApJ, 247, 823
Tolstoy, E., Hill, V., & Tosi, M. 2009, ARA&A, 47, 371
Tremonti, C. A., Heckman, T. M., Kauffmann, G., et al. 2004, ApJ, 613, 898
Valcke, S., de Rijcke, S., & Dejonghe, H. 2008, MNRAS, 389, 1111
van Zee, L., Skillman, E. D., & Salzer, J. J. 1998, AJ, 116, 1186
Verbeke, R., De Rijcke, S., Koleva, M., et al. 2014, MNRAS, 442, 1830
Walcher, J., Groves, B., Budavári, T., & Dale, D. 2011, Ap&SS, 331, 1
Weisz, D. R., Dalcanton, J. J., Williams, B. F., et al. 2011, ApJ, 739, 5
Weisz, D. R., Johnson, B. D., Johnson, L. C., et al. 2012, ApJ, 744, 44
Witt, A. N., & Gordon, K. D. 2000, ApJ, 528, 799
Wright, E. L., Eisenhardt, P. R. M., Mainzer, A. K., et al. 2010, AJ, 140, 1868-1881
Zhao, Y., Gao, Y., & Gu, Q. 2010, ApJ, 710, 663

APPENDIX

SCATTER IN THE M-SFR RELATION

We briefly consider systematic effects and biases across the $M_\star$ and SFR indicators used in this work. As a diagnostic, we start from the assumption that galaxies on the star-forming main sequence (e.g., Brinchmann et al. 2004; Salim et al. 2007) populate a narrow range of star formation rates at a given stellar mass. To assess the quality of of our various $M_\star$ and SFR indicators, we can compare the dispersion about that relation using each combination of the values of $M_\star$ and SFR produced in this work.

In this work, our $M_\star$ estimates include those using simple mass-to-light ratios from monochromatic photometry (in both 3.6μm and K_s), and from our SED fitting analysis (e.g., Figure 8). Our SFR estimates include those from narrow-band Hα photometry and from our SED fitting (e.g., Figure 7).

In order to consistently quantify the scatter in the $M_\star$-SFR relation across different estimators, we first select LVL galaxies which are not identified as early-types or BCDs. In this type of comparison, galaxies with extreme (high or low) star formation properties will add scatter to the main sequence $M_\star$-SFR relation, and should not be included. Additionally, (Salim et al. 2016) found that stellar mass determinations based on UV+optical+MIR SED fits are systematically affected at different sSFRs by ~ 0.1 dex (see their Figure 9).

We also require that galaxies in this comparison have a complete set of observations required to generate these estimates (i.e., fluxes measured at 3.6μm, K_s, Hα, and a best-fitting SED with reduced $\chi^2 < 5$). This yields a common sample of 97 LVL galaxies which we use to compare $M_\star$ and SFR estimates.

Figure 14 shows the $M_\star$-SFR relations for each combination of indicators in this common sample. The top row compares the Hα SFRs with our three estimates of mass (SED-fit, K_s, and 3.6μm), and the bottom row shows the 50-Myr-averaged SFR from our SED fitting. The results of linear least squares fits to the SFR-$M_\star$ relations in each panel are shown, and the RMS scatters are given. Within this sample, the scatter about the fit increases from $M_\star$(3.6μm) to $M_\star(K_s)$ to $M_\star$(SED); and also increases from SFR(Hα) to SFR(SED). The relation with the lowest scatter (0.39 dex) is SFR(Hα) vs $M_\star$(3.6μm), and the SED-fit quantities have the largest scatter (0.50 dex)

Given that the scatter in the SFR-$M_\star$ relation increases when using SED fits, one might question whether the SED-fitting is improving the determination of SFR and $M_\star$ in this analysis. However, the goal of this project is not to simply re-measure SFR and $M_\star$ in normal main sequence star-forming galaxies using standard monochromatic indicators (for works which focus on statistical samples of star-forming galaxies, see Brinchmann et al. 2004; Salim et al. 2007, 2016, and references therein). Rather, we are adopting a consistent SED-fitting methodology in order to determine SFR and $M_\star$ even when considering more extreme galaxies which have not previously been included in calibrating $M_\star$ and SFR indicators. This approach allows us to quantify the differences between BCDs (with extreme star formation) and the population of main sequence star-forming galaxies, using consistent estimates of SFR and $M_\star$.

Strong and/or recent star formation can bias monochromatic stellar mass estimates of galaxies. For example, if a dwarf galaxy undergoes a strong starburst, some of its K_s and 3.6μm luminosity will come from the young stellar populations and those monochromatic estimates of stellar mass could be systematically larger than for an otherwise similar passive (or normal star-forming) galaxy.

Also note the relative positions of the four LVL galaxies classified as BCDs (black stars) on the top row of the Figure 14. In each panel those four galaxies have the same SFR(Hα), but their $M_\star$ values are different. When using 3.6μm or K_s luminosity to estimate $M_\star$, these four galaxies are closer to the best-fit main sequence line for normal galaxies. However, if the full SED-fitting is used, their $M_\star$ estimates are reduced – it appears that their strong star formation events may be artificially enhancing their 3.6μm and K_s stellar masses.

By including UV, optical, and IR photometry, our SED-fits produce more robust $M_\star$ and SFR estimates for our diverse sample of galaxies which have a wide range of star formation histories. This systematic and consistent approach allows us to compare BCDs with a large sample of "normal" galaxies, without a bias toward main-sequence star-forming systems.

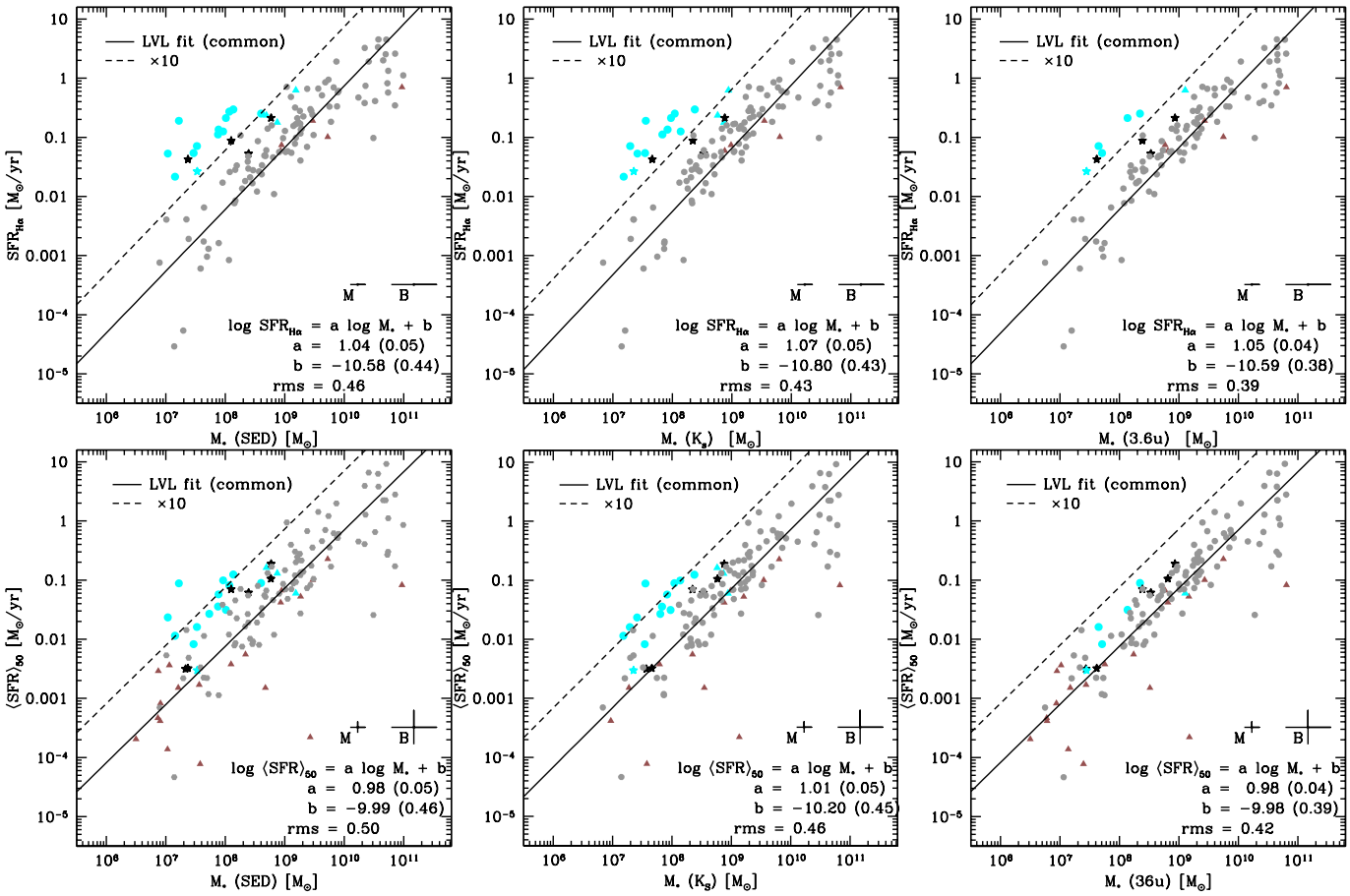
LVL fit (common)
×10
log SFR$_{Hα}$ = a log M$_⋆$ + b
a = 1.04 (0.05)
b = −10.58 (0.44)
rms = 0.46
M. (SED) [M$_⊙$]
SFR$_{Hα}$ [M$_⊙$/yr]
log SFR$_{Hα}$ = a log M$_⋆$ + b
a = 1.07 (0.05)
b = −10.80 (0.43)
rms = 0.43
M. (K$_s$) [M$_⊙$]
log SFR$_{Hα}$ = a log M$_⋆$ + b
a = 1.05 (0.04)
b = −10.59 (0.38)
rms = 0.39
M. (3.6u) [M$_⊙$]
⟨SFR⟩$_{50}$ [M$_⊙$/yr]
log ⟨SFR⟩$_{50}$ = a log M$_⋆$ + b
a = 0.98 (0.05)
b = −9.99 (0.46)
rms = 0.50
M. (SED) [M$_⊙$]
log ⟨SFR⟩$_{50}$ = a log M$_⋆$ + b
a = 1.01 (0.05)
b = −10.20 (0.45)
rms = 0.46
M. (K$_s$) [M$_⊙$]
log ⟨SFR⟩$_{50}$ = a log M$_⋆$ + b
a = 0.98 (0.04)
b = −9.98 (0.39)
rms = 0.42
M. (36u) [M$_⊙$]

FIG. 14.— Each panel shows SFR vs $M_\star$ for a common sample of 97 late-type (non-BCD) galaxies from LVL. This common sample is plotted with grey dots and its best-fit parameters are given for linear least squares fitting. Also shown (but not included in the fits) are members of our BCD sample (cyan dots), our BCD/Es (cyan triangles), BCDs from the LVL sample (black stars), and early-type galaxies from the LVL sample (red triangles). Our results for Mk 475 are shown as a cyan star. The RMS scatter about the main sequence is largest for the SED-derived $M_\star$(SED) vs $\langle SFR\rangle_{50}$ relation, and lowest for the $M_\star(3.6\mu m)$ vs $SFR_{H\alpha}$ relation.